



**HAL**  
open science

# The downward transport of momentum to the surface in idealized sting-jet cyclones

Gwendal Rivière, Didier Ricard, Philippe Arbogast

► **To cite this version:**

Gwendal Rivière, Didier Ricard, Philippe Arbogast. The downward transport of momentum to the surface in idealized sting-jet cyclones. *Quarterly Journal of the Royal Meteorological Society*, 2020, 146 (729), pp.1801-1821. 10.1002/qj.3767 . hal-02920016

**HAL Id: hal-02920016**

**<https://hal.science/hal-02920016>**

Submitted on 8 Dec 2023

**HAL** is a multi-disciplinary open access archive for the deposit and dissemination of scientific research documents, whether they are published or not. The documents may come from teaching and research institutions in France or abroad, or from public or private research centers.

L'archive ouverte pluridisciplinaire **HAL**, est destinée au dépôt et à la diffusion de documents scientifiques de niveau recherche, publiés ou non, émanant des établissements d'enseignement et de recherche français ou étrangers, des laboratoires publics ou privés.

3 **The downward transport of momentum to the**  
4 **surface in idealized sting-jet cyclones**

5 **Gwendal Rivière<sup>1</sup> | Didier Ricard<sup>2</sup> | Philippe**  
**Arbogast<sup>3</sup>**

6 <sup>1</sup>LMD/IPSL, École Normale Supérieure, PSL  
Research University, Sorbonne Université,  
École Polytechnique, CNRS, Paris, France

Processes leading to the formation of strong surface wind

<sup>2</sup>CNRM, Université de Toulouse,  
Météo-France, CNRS, Toulouse, France

<sup>2</sup>Météo-France, Toulouse, France

**Correspondence**

G. Rivière, LMD/IPSL, Ecole Normale  
Supérieure, 24 Rue Lhomond, 75231 Paris  
Cedex 05, France  
Email: griviere@lmd.ens.fr

**Funding information**

gusts within an idealized sting-jet extratropical cyclone are investigated using a high-resolution mesoscale model. It is motivated by real case studies that have shown that damaging surface winds ahead of the bent-back warm front of an extratropical cyclone are often due to the presence of a sting jet, which is a low-level mesoscale jet whose air masses descend from the cloud head to the top of the boundary layer. Different numerical simulations show that surface winds below the leading edge of the sting jet increase with increased horizontal resolution and surface roughness. For typical land surface roughness, the intensity of the near-surface wind gusts rapidly increases with horizontal resolution while the sting-jet intensity above the boundary layer does not vary with resolution. A focus on the 1-km grid-spacing simulation with land surface roughness is then made. It shows stronger surface winds ahead of the bent-back warm front than near the cold-conveyor-belt jet. It also exhibits multiple bands of strong surface wind speed similarly to real sting-jet cyclones. These multiple bands are closely linked with multiple resolved convective rolls in the boundary layer whose descending branches are responsible for the downward transfer of momentum. Sensitivity experiments and a stability analysis show that the cooling due to sublimation and melting of precipitating ice hydrometeors below the leading edge of the sting jet trigger and invigorate the boundary-layer convective rolls by reducing the buoyancy of air masses near the precipitation base and below. Closer to the surface, the transfer of momentum is predominantly taken over by subgrid-scale turbulent fluxes.

#### KEYWORDS

Sting-jet, wind, gust, bent-back warm front, convective rolls, evaporating precipitation

7

## 8 1 | INTRODUCTION

9 Damaging surface winds inside extratropical cyclones may happen in different regions relative to the cyclones center  
10 and may originate from different dynamical processes. Moderate to strong winds may occur ahead of the cold front

11 along the warm conveyor belt when the cyclone develops toward its mature stage (Browning and Pardoe, 1973; Grønås,  
12 1995; Lackmann, 2002). Another source of strong winds is the cold-conveyor-belt jet (CCBJ) in the vicinity of the warm  
13 front as it wraps cyclonically around the cyclone center (Carlson, 1980; Browning, 1990; Schultz, 2001). At a later stage,  
14 in the so-called Shapiro-Keyser cyclone types (Shapiro and Keyser, 1990), damaging winds may occur southwestward of  
15 the cyclone center along the cold conveyor belt (CCB) or south of the cyclone center ahead of the CCB in the presence  
16 of a sting jet (hereafter denoted as SJ; see Figs. 1, 2 of Hewson and Neu, 2015; Hart et al., 2017; Schultz and Browning,  
17 2017, for an illustration). The SJ phenomenon has been introduced by Browning (2004) when studying the Great  
18 Storm of October 1987 that led to huge damages in northwest France and southeast England. The SJ is a mesoscale jet  
19 above the CCB jet associated with air masses descending from the cloud head in the midtroposphere to the top of the  
20 boundary layer. Then, boundary-layer processes help to transfer high momentum down to the surface. Most studies on  
21 SJ analyzed real wind storms in the North Atlantic sector (Clark and Gray, 2018) but this does not mean that it does not  
22 occur in other storm-track regions. For instance, a recent paper by Brăncuș et al. (2019) showed the occurrence of a SJ  
23 in a Mediterranean extratropical cyclone. Very few studies directly observed SJs or their effects at the surface. Parton  
24 et al. (2009) observed the detailed vertical structure of the SJ of windstorm *Jeanette*, thanks to the VHF wind profiler at  
25 Aberystwyth. Direct airborne in-situ measurements of SJ were made during the DIAMET campaign for Friedhelm storm  
26 (Baker et al., 2013; Martinez-Alvarado et al., 2014a; Vaughan et al., 2015). The CCB jet and SJ were shown to merge in  
27 some regions even though the associated air streams had different origins. More recently, 1-minute resolution wind  
28 measurements made with the Chibolton Doppler radar provided information on the downward transfer of momentum  
29 from the SJ toward the surface in the St-Jude storm (Browning et al., 2015).

30 There are no climatologies of directly detected SJs and very few climatologies of SJ precursors exist. The resolution  
31 of models producing reanalysis data being too coarse to represent mesoscale jets like sting jets only indirect information  
32 on the existence of SJ can be provided through the detection of large-scale precursors (Martinez-Alvarado et al., 2012;  
33 Hart et al., 2017). The first climatology by Martinez-Alvarado et al. (2012) (see also Martinez-Alvarado et al., 2014b)  
34 showed that a third of 100 intense storms in the North Atlantic exhibited SJ precursors. This proportion was confirmed  
35 by the more extensive climatology from Hart et al. (2017) based on seasons from 1979 to 2012 with a slightly greater  
36 percentage found for explosively developing cyclones than nonexplosively developing cyclones. Also, SJ cyclones  
37 represent 42% of the population of explosively cyclones and half of the strong wind cyclones crossing the British  
38 Isles. A recent study by Martinez-Alvarado et al. (2018) showed that the number of cyclones exhibiting the sting-jet  
39 precursors increases from 32% to 45% between present-day and future climate simulations under the most extreme  
40 climate-change scenario.

41 Most existing studies on SJs investigated mechanisms for the formation of SJs. Since SJ air masses exhibit slantwise  
42 descending motions, the release of conditional symmetric instability (CSI Bennetts and Hoskins, 1979; Schultz and  
43 Schumacher, 1999) was first hypothesized to play a key role in these motions by Browning (2004). Since then, different  
44 diagnostics have been applied to check the relevance of CSI such as the downdraft slantwise convective available  
45 potential energy (Gray et al., 2011) or the saturated moist potential vorticity (Martinez-Alvarado et al., 2010; Baker  
46 et al., 2014; Martinez-Alvarado et al., 2014a; Coronel et al., 2016; Volonté et al., 2018). Most studies found evidence  
47 of unstable conditions for CSI within the cloud head in the upstream region of the descending SJ air masses (Gray  
48 et al., 2011; Baker et al., 2014; Martinez-Alvarado et al., 2014a; Volonté et al., 2018), and Volonté et al. (2018) also  
49 showed evidence of unstable conditions for symmetric and inertial instabilities. Coronel et al. (2016) identified neutral  
50 conditions for CSI in their idealized SJ cyclones but this could be the signature of already released CSI according to  
51 Clark and Gray (2018). It is likely that real SJ cyclones exist without being strongly unstable to CSI (Smart and Browning,  
52 2014; Clark and Gray, 2018). Another branch of studies made an emphasis on the role played by balanced dynamics.  
53 Regions of SJ descents are co-located with geostrophically-forced descending motions as diagnosed by the divergence

of the Q-vector (Coronel et al., 2016; Slater et al., 2017) and could be in large part connected to the frontolytic descent in the SJ region (Schultz and Sienkiewicz, 2013; Slater et al., 2015, 2017). The strong horizontal wind speed occurring in the co-located regions of the CCB jet and SJ southwest and south of a Shapiro-Keyser cyclone are mainly due to the along-flow pressure gradient force (Slater et al., 2015) or equivalently the pressure work (Rivière et al., 2015b). A third potential mechanism is the evaporative cooling that could reinforce both the SJ descent and horizontal wind speed but idealized and more realistic simulations showed that its effect is rather weak (Baker et al., 2014; Coronel et al., 2016; Smart and Browning, 2014). The review paper by Clark and Gray (2018) concluded that there is a continuum of mechanisms explaining the presence of SJ in which the balanced descents associated with synoptic-scale dynamics can be reinforced by mesoscale moist instabilities like CSI.

One aspect which has been less studied is the dynamics of downward transfer of high momentum from the sting jet to the surface (Clark and Gray, 2018). Strong surface winds between the head of the bent-back warm front and the cold front might be due to the presence of the CCB jet or SJ or both (Smart and Browning, 2014). Analyzing satellite imagery from Meteosat, Browning and Field (2004) identified different arc-shaped and chevron-shaped clouds within the boundary layer of the Great Storm of October 1987 suggesting the presence of boundary-layer convergence lines ahead of the downward transport of momentum. Most studies showed that regions of strong surface winds below SJs were collocated with regions of weak boundary-layer static stability. For instance, Clark et al. (2005) found that below SJs, the wet-bulb potential temperature was quite constant leading to neutral conditions for moist convection. In another context, Kelley et al. (2019) showed that the momentum of an elevated jet of a lee cyclone can be brought down to the surface where the static stability below is neutral to unstable. However, in most places, the top of the boundary layer just below SJs is characterized by enhanced static stability as seen in observed cases (Browning and Field, 2004) and idealized cases (Baker et al., 2014; Coronel et al., 2016). What is happening near the top of the boundary layer in a region of strong vertical shear is still unclear (Clark and Gray, 2018). Within the boundary layer, ahead of the bent-back warm front, the static stability is probably reduced compared to other regions which seems to favor the transfer of momentum by convective rolls (Clark et al., 2005; Schultz and Sienkiewicz, 2013; Browning et al., 2015; Hewson and Neu, 2015; Slater et al., 2017). In their study of the St-Jude storm, Browning et al. (2015) identified different convective cells some of them being shallow and confined in the boundary layer, some others being more elevated. They also emphasize the importance of evaporative precipitation residues and showers in bringing down high momentum to the surface. Finally, Slater et al. (2017) showed how surface fluxes destabilize the boundary layer and help transferring momentum down to the surface. The present study aims at investigating processes responsible for the downward transfer of momentum within the same idealized framework as that of Coronel et al. (2016) which does not contain any surface fluxes.

In order to simulate idealized sting jets, it is necessary to get a bent-back warm front which is likely to form in cyclones crossing the slowly-varying large-scale jet (Rivière et al., 2015a,b; Coronel et al., 2016). It also requires enough horizontal and vertical resolutions. A 10-km grid-spacing simulation is usually enough to represent SJs and most numerical studies have used this kind of resolution (see table 3 of Clark and Gray, 2018). An appropriate ratio between the vertical and horizontal grid spacings of about 1/50 were also mentioned to be the key to correctly simulate SJ and their associated slantwise descending motions (Persson and Warner, 1993; Lean and Clark, 2003; Clark et al., 2005). However, in Coronel et al. (2016), this ratio was not found to be crucial once the horizontal resolution is high enough. Only three studies have looked at better horizontal grid spacing than 10 km: 7-km in Martinez-Alvarado et al. (2010), 5-km in Smart and Browning (2014) and 4-km in Coronel et al. (2016). In the present study, we will decrease the grid spacing to 1 km. The aim is to resolve boundary-layer convective rolls of few kilometers similar to those described for the St-Jude storm by Browning et al. (2015).

The paper is organized as follows. The model and setup of the simulations are presented in section 2. Section 3 is

dedicated to the results. It includes analysis of sensitivity experiments for which the horizontal grid spacing and surface roughness are changed. The way high momentum is transferred downward is analyzed by computing passive tracers and by separating the downward momentum fluxes into subgrid-scale and resolved components. The effect of evaporative cooling is then studied by turning off this process in one simulation. Finally, instability criteria facilitating mixing are computed such as the Richardson number and the criterion for cloud-base detrainment instability. A summary of the results is provided in section 4.

## 2 | METHOD

### 2.1 | Model

The model used to simulate the idealized SJ cyclone is the non-hydrostatic mesoscale research model Meso-NH (Lafore et al., 1998; Lac et al., 2018). It has the same configuration as in Coronel et al. (2016). It includes the one-moment bulk-cloud microphysical scheme ICE3 of Pinty and Jabouille (1998) with five prognostic hydrometeors (cloud droplets, rain, ice crystals, snow and graupel mixing ratios, in addition to water vapour). Subgrid-scale transports are parametrized by the mass-flux scheme for deep convection of Bechtold et al. (2001) and a 1.5-order closure scheme for turbulence (Cuxart et al., 2000) with the turbulence mixing length formulation of Bougeault and Lacarrère (1989). Surface conditions are specified at the lower boundary with a prescribed roughness length. There is no radiation scheme, the surface sensible and latent heat fluxes are set to zero and the shallow convection scheme is disabled.

### 2.2 | Set up of simulations

The model domain is 10 000 km long in the zonal direction and 6000 km wide in the meridional direction (Figure 1(a)). The vertical extension is 16 km. Zonal boundaries are cyclic and the northern and southern boundaries have wall boundary conditions. The vertical resolution has an irregular vertical level spacing and increases with altitude. It is fixed for all simulations of the present study and corresponds to 50-150 m spacing between the ground and 2 km altitude, 150-290 m between 2 and 5 km altitude and 290-430 m between 5 and 8 km.

A 20-km grid-spacing simulation is first performed over the whole domain up to  $t = 96$  h starting from the same initial conditions as those shown in Figure 1 of Coronel et al. (2016). The simulation is denoted S20sea\_parent and its state at  $t = 72$  h is used to initialize the other simulations described in the present paper (Figure 1(a)). S20sea\_parent has a roughness length of  $2 \times 10^{-4}$  m corresponding to a typical value for sea surface. The initial flow consists of a zonal baroclinic jet and two synoptic-scale disturbances located near the tropopause and the surface. The jet axis is located halfway between the southern and northern boundaries and the two disturbances are located south of the jet axis which is a favorable condition to form a Shapiro-Keyser cyclone (Rivière et al., 2015a,b). During their evolution, the two disturbances baroclinically interact with each other and the zonal jet. A deep surface cyclone forms, crosses the jet axis and reaches a maximum deepening of about 940 hPa once located north of the jet axis after 3 to 4 days (Figure 1(a)).

Two sets of three simulations with 20-km, 4-km and 1-km grid spacings are then performed. Only the 20-km grid-spacing simulation uses the mass-flux scheme for deep convection as convective motions are explicitly resolved for the 4-km and 1-km grid-spacing simulations. For the first set, the roughness length is  $2 \times 10^{-4}$  m corresponding to typical sea surface. The associated three simulations are respectively called S20sea, S4sea and S1sea. S20sea and S4sea are initialized with the S20sea\_parent state at  $t = 72$  h (Figure 1(a)) and last until  $t = 96$  h. S20sea is run over the large domain and S4sea over the red square domain shown in Figure 1(a). The red square domain is chosen to include the mature stage of the cyclone during which a SJ is formed and the seclusion stage occurs (Coronel et al., 2016). The

**TABLE 1** List of simulations

Simulations	grid spacing	Roughness	Suppressed processes	two-way nesting
S20sea_parent	20 km	0.0002	none	no
S20sea	20 km	0.0002	none	yes
S4sea	4 km	0.0002	none	yes
S1sea	1 km	0.0002	none	yes
S20land	20 km	0.01	none	yes
S4land	4 km	0.01	none	yes
S1land	1 km	0.01	none	yes
S1land_nocl	1 km	0.01	no evaporative cooling from precipitation	yes
S1land_nocl_noevap	1 km	0.01	no evaporative cooling and no evaporation	yes

interactions between the S20sea and S4sea simulations is made using a two-way nesting, meaning that both simulations run at the same time and exchange information in both directions, to obtain the most accurate state for S4sea. S20sea and S4sea are the same as the low-high and high-high resolution simulations discussed in Coronel et al. (2016). S1sea is performed from  $t = 84$  h to 96 h and nested in the domain shown by the black square in Figure 1. To get S1sea, a 20-km grid spacing run is performed over the whole domain, interacting with a 4-km grid-spacing run in the red domain, which itself interacts with a 1-km grid spacing run in the black domain from  $t = 84$  h to 96 h. The latter run is called S1sea.

Exactly the same procedure is applied for the second set of 20-km, 4-km and 1-km grid-spacing simulations for which the roughness length is set to  $10^{-2}$  m corresponding to a typical smoothed land surface. The runs are respectively called S20land, S4land and S1land and are performed in the same domains as S20sea, S4sea and S1sea, respectively. The choice of the 1-km grid spacing domain is such that it includes the southern part of the cyclone during the time interval between  $t = 84$  h and 96 h. During that time interval, the domain contains a low-level jet above the boundary layer at  $z = 2$  km that moves from the southwest to the south of the cyclone center, that is, between the leading edge of the bent-back warm front and the cold front (Figures 1(b),(c)). This low-level jet has been identified as being a SJ in Coronel et al. (2016). Indeed, backward trajectories starting from the wind maximum at  $z = 1.8$  km to the south of the cyclone center at  $t = 96$  h confirm that the air masses have undergone rapid descending motions from the cloud head situated at  $z = 3.5$  km with increased wind speed and dryness.

A last set of two simulations is performed in the black square domain from  $t = 84$  h to 96 h. S1land\_nocl is the same simulation as S1land but for which the evaporative cooling from precipitating hydrometeors (rain, graupel, and snow) is turned off but the conversion into vapour is allowed to happen. S1land\_nocl\_noevap is the same simulation as S1land but both the evaporative cooling and evaporation transition are suppressed. Table 1 summarizes all the experiments analysed in the present paper.

### 3 | RESULTS

#### 3.1 | Resolution effects and roughness effects

Figure 2 shows the horizontal wind speed above the boundary layer at  $z = 1.6$  km and the cloud structure at  $t = 93$  h for S20land, S4land and S1land. The SJ extends from the west to the south of the cyclone center and reaches a maximum

160 value of about  $42 \text{ m s}^{-1}$  at  $x = 8400 \text{ km}$ ,  $y = 3000 \text{ km}$  for the three simulations. A secondary maximum of the SJ is also  
161 visible for the three simulations near the cloud head with values around  $37 \text{ m s}^{-1}$ . To conclude on Figure 2, there is no  
162 major difference in the amplitude and location of the SJ between the different horizontal grid spacings. As noticed in  
163 Coronel et al. (2016), differences appear when the vertical grid is too coarse and the structure of the SJ disappears for a  
164 500-m vertical grid spacing.

165 Near the surface, at  $z = 25 \text{ m}$ , a local maximum of horizontal wind speed of about  $23 \text{ m s}^{-1}$  appears below the  
166 maximum wind speed of the SJ and CCB jet at roughly  $x = 8450 \text{ km}$ ,  $y = 3100 \text{ km}$  for all resolutions (Figures 3(a),(c),(e)).  
167 This maximum is located 100 km southwest of the bent-back warm front. More downstream, for the 20-km grid spacing,  
168 the wind speed continuously decreases (Figure 3a) whereas for the 4-km and 1-km grid spacings, bands of wind speed  
169 maxima appear in a region of weak thermal contrasts around  $x = 8900 \text{ km}$  (Figures 3(c),(e)). For the 1-km grid spacing,  
170 wind speed maxima in these bands reach values as high as  $26 \text{ m s}^{-1}$  which is stronger than the upstream maximum near  
171 the bent-back warm front.

172 The different bands of wind speed maxima for S4land and S1land have a rather barotropic structure in the boundary  
173 layer. They correspond to descending air masses starting a bit below the SJ, which is located around  $z = 1.5 \text{ km}$ , and finish  
174 near the surface. These descending regions are separated by ascending ones with local wind speed minima (Figures  
175 3(d),(f)). In S1land, the alternating resolved ascents and descents have typical intensities of about  $0.5 \text{ m s}^{-1}$  and typical  
176 wavelength of 5-20 km. The correlation between the vertical velocity and the horizontal wind speed in the region where  
177 these bands of wind speed maxima appear and inside the boundary layer is rather high: it varies between 0.6 and 0.8  
178 depending on the region. In S4land, the ascents and descents are 2 to 3 times weaker than in S1land and the typical  
179 wavelength is about 20 km or larger. In S20land, some bands of wind speed maxima are only slightly visible and their  
180 associated vertical motions are much weaker than for the other two simulations (this is the reason why no contour  
181 appears in Figure 3b). The peaks of vertical motions in S20land are roughly 3 times smaller than those of S4land. To  
182 conclude on the land surface roughness simulations, the intensity of the near-surface wind gusts below the leading edge  
183 of the sting jet rapidly increases with horizontal resolution while the sting-jet intensity above the boundary layer does  
184 not vary with resolution.

185 For the simulations with typical sea surface roughness (Figure 4), the multiple near-surface wind speed maxima  
186 farther ahead of the bent-back warm front are less intense and much less visible than those with typical land roughness.  
187 For S20sea (Figures 4(a),(b)), they are almost absent; for S4sea they start to appear (Figures 4(c),(d)) and for S1sea  
188 (Figures 4(e),(f)) they are visible but less intense than for S1land. On the contrary, the maximum along the CCB jet  
189 near  $x = 8400 \text{ km}$ ,  $y = 3100 \text{ km}$  is greater for S20sea, S4sea and S1sea than for S20land, S4land and S1land and  
190 reaches values close to  $32 \text{ m s}^{-1}$  as a result of a weaker friction near the surface. The SJ is also stronger for sea surface  
191 roughness than land surface roughness, about  $40 \text{ m s}^{-1}$  for the former and  $36 \text{ m s}^{-1}$  for the latter along the cross section  
192 AA'. Another interesting difference is that along the same cross section, the CCB jet is still visible for sea roughness  
193 simulations and not at all for land surface simulations. Finally, even though S1sea exhibits alternating bands of local  
194 maxima and minima in wind speed along AA', the maxima are still significantly weaker than the large-scale maximum  
195 along the CCB jet.

196 For all simulations performed with a sea surface roughness, the global maximum wind speed found at the surface  
197 was along the CCB jet and not farther ahead of it as in Coronel et al. (2016). It is only in the case of the 1-km grid-spacing  
198 simulation with land roughness that maxima ahead of the CCB jet are stronger than the maximum located along the  
199 CCB jet. Both the resolution and the roughness are responsible for setting the maximum wind speed in the region of  
200 weak thermal contrasts between the head of the bent-back warm front and the cold front.

201 The evolution of multiple bands of near-surface wind speed maxima for S1land is shown in Figure 5 between  $t = 91 \text{ h}$   
202 and  $t = 96 \text{ h}$ . Between  $t = 91 \text{ h}$  and  $t = 93 \text{ h}$  (Figures 5(a)-(f)), many bands such as those inside or near the yellow squares



are located below the leading edge of the SJ at  $z = 1.6$  km. Some others are more to the northeast of the SJ main core region as those located in the domain  $x = 8800\text{--}8900$  km and  $y = 2900\text{--}3000$  km at  $t = 91.5$  h (Figure 5(b)). They also appear below high values of wind speed at  $z = 1.6$  km but the values are weaker than below the SJ main core region. We noticed that on its northeastern flank the SJ is very thin in the vertical direction and peaks around  $z = 1.5$  km. This small vertical extension is well visible in Figure 3(f) close to A' between  $y = 2900$  km and  $y = 3000$  km while the SJ is deeper and more intense south of  $y = 2900$  km. So most of the bands of wind speed maxima are found below the leading edge of the SJ but not necessarily where the sting jet is the strongest. Between  $t = 94$  h and  $t = 96$  h (Figures 5(g)-(i)), small-scale bands of near-surface wind speed maxima appear roughly 100 km upstream of the previously described ones (see e.g., near  $x = 8700$  km  $y = 2850$  km at  $t = 94$  h). These newly created bands appear below the leading edge of another wind speed maximum at the SJ level ( $z = 1.6$  km) which is visible in the figure from  $t = 92$  h. Between  $t = 92$  h and  $t = 96$  h, we clearly see two large-scale wind speed maxima within the SJ region: the first bands of near-surface wind speed maxima are located below the first SJ maximum while the second bands below the leading edge of the second SJ maximum. The origins of these two types of bands are hereafter analyzed.

### 3.2 | The distinct role of subgrid-scale and resolved circulations in downward transfer of momentum

To check that part of the air masses reaching the surface is indeed coming from the sting jet, passive tracers are initialized from  $t = 90$  h to  $t = 93$  h at the grid point  $x = 8550$  km  $y = 2800$  km and its 8 adjacent neighbours between  $z = 1.5$  km and 2.0 km. This grid point was chosen by using backward Lagrangian trajectories starting at  $t = 93$  h in the free troposphere just above a particular near-surface wind speed maximum at  $x = 8920$  km  $y = 2820$  km (not shown). Figure 5 shows the evolution of the passive tracer at the level of the SJ ( $z = 1.6$  km). At  $t = 91$  h, the leading edge of the green contour is in a region of maximum wind speed of the SJ while at  $t = 93$  h it is more ahead of it. The eastward advection of the passive tracer is thus faster than the displacement of the SJ wind speed maxima.

Figure 6 exhibits a zoom of the evolution of the passive tracer. At  $t = 91$  h (Figure 6(a)), there is no trace of the passive tracer in the boundary layer. At  $t = 91.5$  h, a first pinch of passive tracer appears in the middle of the boundary layer around  $x = 8690$  km  $y = 2790$  km (see blue shadings in Figure 6(b)). The passive tracer content entering the boundary layer locally increases with time as seen around  $x = 8740$  km  $y = 2795$  km at  $t = 92$  h (Figure 6(c)) and  $x = 8770$  km  $y = 2800$  km at  $t = 92.25$  h (Figure 6(d)). Downstream of this peak in passive tracer content, one can easily see a local maximum in horizontal wind speed at  $z = 200$  m located around  $x = 8720$  km  $y = 2790$  km at  $t = 91.5$  h,  $x = 8775$  km  $y = 2800$  km at  $t = 92$  h and  $x = 8800$  km  $y = 2805$  km at  $t = 92.25$  h. This maximum increases with time between  $t = 91.5$  h and  $t = 92$  h and then keeps constant until  $t = 93$  h.

At  $t = 92.25$  h (Figure 6(d)), a second pinch of passive tracer enters the middle of the boundary layer at  $x = 8810$  km  $y = 2800$  km in connection with a local wind speed maximum located more downstream. Fifteen minutes later (Figure 6(e)), this new intrusion of passive tracer forms a long zonal band extending from  $x = 8790$  km to  $x = 8860$  km which terminates into two small branches, one near the previously mentioned wind speed maximum at  $x = 8850$  km  $y = 2805$  km and a more intense wind speed maximum at  $x = 8880$  km  $y = 2805$  km. The latter maximum slightly increases with time from  $t = 91.5$  h to  $t = 92.5$  h (Figures 6(b)-(e)) and then slightly decreases between  $t = 92.5$  h and  $t = 93$  h (Figures 6(e)-(f)). All the intrusions of passive tracer within the boundary layer move more rapidly to the north than the passive tracer at the top of the boundary layer because of more intense northward winds within the boundary layer than at the top (not shown).

Figure 7 shows different vertical cross sections at  $t = 92.5$  h in the region of the second burst of downward transport of passive tracer to identify key processes allowing such a downward transport. The cross section  $xx'$  is made along the

244 main direction of the wind in the boundary layer and has been chosen in such a way that it crosses the near-surface wind  
245 maximum located around  $x=8880$  km  $y=2805$  km. Above this near-surface wind maximum, a peak value of downward  
246 momentum fluxes is well visible and located below the edge of high passive tracer content at the top of the boundary  
247 layer (Figure 7(b)). Some passive tracer content has been transported downward by this cell of downward motion but  
248 the amount of passive tracer transported to the surface is rather small: the ratio between the peaks at the surface and  
249 those at the sting jet level is of the order of a few percent (see blue contours in Figure 7). The peak values of passive  
250 tracer near the surface are located upstream of the near-surface wind maximum. This can be explained by the fact that  
251 the eastward displacement of the passive tracer at the SJ level (roughly  $z = 1.5$  km) is more rapid than the eastward  
252 displacement of the convective rolls of the boundary layer. Once the high passive tracer content at the SJ level reached  
253 a cell of downward motion, the passive tracer starts to descend at the western edge of the descending cell. A bit later,  
254 the high passive tracer content at the SJ level covers the whole descending cell and there is therefore more passive  
255 tracer content at the western edge of the descending cell than at the eastern edge. This explains why the peak in passive  
256 tracer content near the surface appears behind the descending cell in Figure 7(b). The same observations can be made  
257 when looking at the latitudinal cross sections of Figures 7(c)-(e): the passive tracer is just starting to descend in the most  
258 eastern section (cc') while it is already much closer to the surface in the most western section (aa'). In the latitudinal  
259 cross sections, the downward intrusion of passive tracer is better co-located with the intense downward momentum  
260 fluxes than in section xx' (Figure 7(b)) because the bands of downward motion are longitudinally oriented and the flow is  
261 mainly zonal. However, there is a slight northward shift of the passive tracer content relative to the downward motion  
262 in the latitudinal cross sections (aa'), (bb') and (cc') because there are slightly more northward winds inside the boundary  
263 layer compared to the top as noticed in the previous paragraph. In all cross sections, a good co-location of regions of  
264 high wind speed and downward momentum fluxes in the boundary layer is seen. Finally, turbulent fluxes are more active  
265 very near the surface where they are homogeneously oriented downward and reach values as large as the resolved  
266 fluxes below  $z=500$  m (see shadings in Figure 7(a)). The comparison between the black contours of Figures 7(a) and  
267 (c), which represent the resolved and total momentum fluxes respectively, shows that the subgrid-scale fluxes have a  
268 significant contribution to the downward transfer of momentum in the first hundred meters of the atmosphere only.

269 To better quantify the relative roles of the resolved and subgrid-scale fluxes, Figure 8 shows their average in two  
270 distinct regions of the boundary layer at  $t = 92.5$  h, one located near the bent-back warm front (pink square in Figure  
271 5(e)) and the other further downstream below the leading edge of the SJ (yellow square in Figure 5(e)). The averages  
272 are made in these two regions only where the horizontal wind speed near the surface ( $z = 200$  m) exceeds  $28 \text{ m s}^{-1}$   
273 in order to focus on the downward transport of high momentum. In the downstream region, such a selection leads  
274 to a wind profile with a peak near  $z = 400$  m as seen in the red curve of Figure 8(a). In the downstream region, the  
275 subgrid-scale fluxes are an order of magnitude smaller than the resolved ones at altitude higher than 300 m. Below 300  
276 m, the resolved fluxes become smaller and smaller closer to the surface while the subgrid-scale fluxes become more and  
277 more intense. In that region, it is only in the last 50 m above the surface that the subgrid-scale fluxes dominate in the  
278 downward transport of momentum. In the upstream region, the wind profile monotonically increases with height in the  
279 boundary layer (red curve in Figure 8(b)) and the amplitude of the resolved momentum fluxes is seven times as small as  
280 the same quantity in the downstream region. Because the resolved fluxes are much less intense in the upstream region  
281 and because the subgrid-scale fluxes are stronger at higher altitude, the role played by the latter fluxes is relatively  
282 more important in the upstream region than in the downstream one. The sum of the two fluxes, corresponding to the  
283 total transport of momentum, is much larger in the downstream region than in the upstream one because of the large  
284 difference in the resolved fluxes. This explains why there is higher momentum closer to the surface in the downstream  
285 region despite a weaker SJ there (compare the red curves in Figures 8(a),(b)).

286 To conclude, at the leading edge of the SJ, the downward transfer of momentum occurs sporadically through bursts

of resolved downward circulations starting near the top of the boundary layer. In the lowest part of the boundary layer, below 100 m of altitude, it mainly occurs through subgrid-scale turbulent fluxes.

### 3.3 | Effect of evaporative cooling from precipitating hydrometeors

As mentioned in the introduction, the role of evaporative cooling in the intensity of the descent and horizontal wind speed of the SJ has been quantified in the idealized simulations of Baker et al. (2014) and Coronel et al. (2016) by turning off the evaporative cooling. In both cases, the impact was shown to be negligible or small. For instance, the effect does not exceed  $2 \text{ m s}^{-1}$  within the core of the SJ. Evaporative cooling process has also been hypothesized to be the key process for the downward transfer of momentum from the SJ down to the surface by Browning et al. (2015). The idea is that evaporative cooling of precipitation residues could decrease the buoyancy of air masses near the top of the boundary layer and help the air masses to descend and bring down high momentum all the way to the surface. Figure 9(b) shows that precipitation maxima occur in regions of local minima of horizontal wind speed at the top of the boundary layer at  $z = 1.0 \text{ km}$ , in agreement with Vaughan et al. (2015). However, closer to the surface, the peaks in precipitation gets closer to the peaks of wind speed as seen for instance at  $z = 0.5 \text{ km}$  from abscissa 180 to 220 km. The role of evaporative cooling of these precipitation residues in the wind acceleration nearby is questioned.

To test the hypothesis of the role of evaporative cooling in the downward transport of momentum inside the boundary layer, S1land\_nocl has been performed in which the evaporative cooling from precipitating hydrometeors (rain, snow, graupel) has been turned off at  $t = 84 \text{ h}$ . Since the sum of snow and graupel largely dominates over rain, the suppressed cooling is mainly due to the sublimation and melting of solid precipitation. The impact is indeed quite large in the bands of maximum wind speed near the cloud head at the boundary-layer level. Almost all the bands of wind gusts of about  $32\text{--}36 \text{ m s}^{-1}$  located along a moderate-intensity near-surface cold front are suppressed (see the axis BB' in Figures 9(a),(b) and compare with Figures 9(c),(d)). The cold front disappears in that region and the temperature is more homogeneous when the evaporative cooling of precipitating hydrometeors is turned off (compare the black contours in Figures 9(a) and (c)). The sensitivity run S1land\_nocl clearly shows that evaporative cooling of the leading edge of the boundary-layer cloud head and its associated precipitation is an important process for the formation of multiple bands of wind gusts. On the contrary, the wind speed maximum within the CCB jet increases by up to  $2\text{--}4 \text{ m s}^{-1}$  (upper-left quadrant of Figures 9(a),(c)). Suppressing the evaporative cooling tends to reinforce the depression (the SLP minimum is  $2 \text{ hPa}$  lower in S1land\_nocl than in S1land) and the winds to the southwest of the cyclone center in the CCB region. There is also a long band of strong wind gust near  $x = 8700 \text{ km}$ ,  $y = 2920 \text{ km}$  that exist in S1land\_nocl and not in S1land. So the suppression of evaporative cooling does not prevent the formation of bands of strong wind gusts but almost entirely suppresses those located at the leading edge of the boundary-layer cloud filaments.

In the simulation where the evaporative cooling is suppressed and the evaporation is prevented (S1land\_nocl\_noevap), precipitation cannot evaporate and therefore reach the ground as seen in Figure 9(f). In that case, the bands of wind gusts along the axis BB' are less numerous than in S1land but do not completely disappear in contrast with S1land\_nocl (compare Figures 9(a) and (e)). Regions where these bands disappear are those located further away from the maximum wind speed of the sting jet, around  $x = 8650\text{--}8800 \text{ km}$  and  $y = 2650\text{--}2750 \text{ km}$  (see Figures 5(f) and 9(a),(b)). More upstream, in the CCB region, surface wind gusts in S1land\_nocl\_noevap are weaker than in S1land\_nocl but slightly stronger than in S1land. The comparison between S1land\_nocl\_noevap and S1land\_nocl indicates that the newly created water vapor via evaporation helps intensifying the winds below the CCB jet but prevents the downward transfer of momentum from the sting jet to the surface at the leading edge of the cloud. The boundary layer is also warmer in S1land\_nocl than in S1land\_nocl\_noevap, especially near the top of the boundary layer (not shown), because it leaves the possibility for the newly created water vapor via evaporation to condense once again.

To conclude, the effect of the evaporating precipitation below the leading edge of the sting jet is twofold. On the one hand, the evaporative cooling itself tends to strongly invigorate the convective rolls within the boundary layer. On the other hand, the newly formed water vapor via evaporation, which can condense once again, acts to diminish the intensity of the rolls. The first effect overwhelms the second effect and the net effect of evaporating precipitation is to multiply the number of convective rolls in the boundary layer and hence to reinforce the downward transfer of momentum at the leading edge of the sting jet. Further insights on the evaporative cooling effect is provided in next section.

### 3.4 | Richardson number, static stability and cloud-base detrainment instability

To determine why the downward transport of high momentum is more efficient below the leading edge of the sting jet than more upstream, different quantities have been computed and shown in Figures 10 and 11. The strategy is first to look at  $t = 90$  h (Figure 10) when convective rolls start to be formed. Three types of quantities are computed to detect favorable conditions for turbulence and instabilities: (i) the Richardson number (or its bulk formula) which provides information on turbulence and mixing activity when it is positive and small and on convective stability when it is negative, (ii) the static stability parameter which more directly provides information on convective instability (iii) a criterion satisfying the cloud-base detrainment instability (CDI) as initially proposed by Emanuel (1981). As shown hereafter, these quantities closely depend on the cooling effect on the buoyancy associated with the sublimation and melting of precipitating ice hydrometeors.

Figure 10(a) shows the Bulk Richardson number  $Ri_B = (g/T_v)(\Delta\theta_v\Delta z)/((\Delta u)^2 + (\Delta v)^2)$  computed at  $t = 90$  h in S1land between  $z = 0.1$  km and  $z = 1.2$  km, where  $g$  is the gravitational acceleration,  $T_v$  is the virtual temperature,  $\Delta\theta_v$  is the virtual potential temperature difference across the chosen layer of thickness  $\Delta z = 1.1$  km, and  $\Delta u$  and  $\Delta v$  are the changes in horizontal wind components across that same layer. The time  $t = 90$  h has been chosen because it is just prior to the occurrence of the convective rolls and we want to check what are the favorable environmental conditions triggering the rolls. A zone of relatively low values of  $Ri_B$  appears below the leading edge of the SJ in the area limited by  $x = 8600$ – $8800$  km and  $y = 2700$ – $2900$  km. This area also corresponds to the separation area between high ice water content (sum of cloud ice, snow and graupel) (zone with green asterisks) and low ice water content. This region of relatively weak  $Ri_B$  is due to lower values of the static stability parameter there and not due to stronger shear. Stronger shears are found in another region more upstream in the vicinity of the bent-back warm front. Therefore, the variations of the static parameter dominates over that of the shear in the Bulk Richardson number of S1land. There is also a region of rather low values of  $Ri_B$  below the leading edge of the SJ in S1land\_nocl (Figure 10(d)) but it is less well localized than in S1land and extends further upstream.

Vertical cross sections  $YY'$  are made inside the area of low values of  $Ri_B$  (Figures 10(b),(d)). They show the local Richardson number ( $Ri = N_v^2/|\partial\mathbf{u}/\partial z|^2$  with  $N_v^2 = (g/\theta_v)(\partial\theta_v/\partial z)$ ) in shadings and the zone of high ice water content (sum of cloud ice, snow and graupel mixing ratios) in green contour. The lower interface between high ice water content and no ice water content is hereafter called the precipitation base because it corresponds to a strong gradient of the sum of snow and graupel mixing ratios. For S1land,  $Ri$  is always negative from the precipitation base to the surface (Figure 10(b)), due to negative static stability parameter  $N_v^2$ . There are some exceptions where convective cells have already formed at  $y = 2720$  km and  $y = 2840$  km. The negative values appearing below the precipitation base can be attributed to the cooling associated with the sublimation and melting of precipitating solid hydrometeors. This is shown by comparing with S1land\_nocl (Figure 10(e)). In a layer of 200 m depth below the precipitation base,  $Ri$  is systematically positive in S1land\_nocl and only becomes negative closer to the surface. The effect of cooling by sublimation and melting of precipitation on the static stability was confirmed by looking at S1land\_nocl\_noevap which does not present strong

369 negative values of static stability below the precipitation base because the evaporative cooling is turned off in that  
 370 simulation too. The reason why S1land\_nocl\_noevap presents more convective rolls than S1land\_nocl (see Figures  
 371 9(c),(e)) might be due to the slightly more negative values of static stability found in the former run compared to the  
 372 latter (not shown). Indeed, the newly formed water vapor via sublimation, can condense again and warm the air masses.  
 373 Such a warming was found to be more important near the top of the boundary layer which has the effect of stabilizing  
 374 the boundary layer in S1land\_nocl compared to S1land\_nocl\_noevap.

375 Farther upstream, along the cross section ZZ', the high values of ice water content are found at a lower altitude due  
 376 to a lower cloud base and lower precipitating hydrometeors (Figures 10(c),(f)). The low values of  $Ri$  are only found in a  
 377 limited layer close to the surface in both runs. However, S1land presents negative values just below the high values of  
 378 ice water content while S1land\_nocl still presents positive values there. As above, this reflects the effect of evaporative  
 379 cooling of precipitating hydrometeors in S1land.

380 Another mechanism for vertical destabilization of the air masses below the leading edge of the sting jet could be the  
 381 destabilization of cloud-base air masses via cloud-base detrainment instability (CDI) as initially introduced by Emanuel  
 382 (1981) to explain mammatus formation. CDI corresponds to an instability of the interface between cloudy air above and  
 383 subsaturated air below. Mixing triggers the instability by bringing cloudy air into the subsaturated environment below  
 384 and the condensate inside the mixed air is evaporated or sublimated. The associated cooling effect helps to decrease  
 385 the buoyancy of the air masses that then extend their descent. Kanak et al. (2008) showed that the CDI criterion is  
 386 necessary to form mammatus and that the sublimation of ice is a key process to get mammatus in their simulations.  
 387 Even though the considered scales are larger in the present case, the configuration is similar with the leading edge of  
 388 the cloud base overlying a region of rather low humidity in the boundary layer. The CDI criterion has been applied here  
 389 as in Kanak et al. (2008) for ice clouds because liquid contents are small compared to solid contents in the present case.  
 390 We define the ice water virtual potential temperature as

$$\theta_{iv} = T_v \left( \frac{p_0}{p} \right)^{\chi} \left( 1 - \frac{q_i}{1 + q_t} \right) \left( 1 - \frac{q_i}{0.622 + q_t} \right)^{\chi-1} \left( 1 - \frac{q_i}{q_t} \right)^{-\gamma} \exp \left( \frac{-L_s q_i}{(C_p + q_t C_{pv}) T} \right), \quad (1)$$

391 and

$$\chi \equiv \frac{R_d + R_v q_t}{C_p + C_{pv} q_t}, \quad (2)$$

392

$$\gamma \equiv \frac{R_v q_t}{C_p + C_{pv} q_t}. \quad (3)$$

393 The ice water virtual potential temperature corresponds to the virtual potential temperature an air parcel would have if  
 394 all ice in the parcel were sublimated.  $q_v$  is the water mixing ratio,  $q_i = q_{snow} + q_{ice} + q_{graupel}$  is the ice water content,  
 395 sum of all ice species,  $q_{snow}$  is the snow mixing ratio,  $q_{ice}$  is the cloud-ice mixing ratio and  $q_t = q_v + q_i$  is the sum of all  
 396 mixing ratios ( $\text{kg kg}^{-1}$ ).  $L_s$  is the latent heat of sublimation ( $\text{J kg}^{-1}$ ),  $T$  is the temperature (K),  $C_p$  is the heat capacity  
 397 at constant pressure for dry air ( $\text{J kg}^{-1} \text{K}^{-1}$ ),  $C_{pv}$  is the heat capacity at constant pressure of vapor ( $\text{J kg}^{-1} \text{K}^{-1}$ ),  $R_d$  is  
 398 the gas constant of dry air,  $R_v$  is the gas constant of water vapor,  $p_0$  is the reference pressure and  $p$  is the pressure.  
 399 Following Emanuel (1994, p220-221) and Kanak et al. (2008) the CDI criterion can be expressed as

$$\Delta\theta_{iv} = (\theta_{iv})_c - (\theta_{iv})_e < 0, \quad (4)$$

where  $c$  and  $e$  refers to the cloud and clear air below the cloud, respectively. In the present case, the criterion is applied everywhere as follows

$$\begin{aligned} \theta_{i_v}(z + \Delta z/2) - \theta_{i_v}(z - \Delta z/2) &< 0, \\ q_i(z + \Delta z/2) &> 5 \cdot 10^{-3} \text{ g kg}^{-1}, \end{aligned} \quad (5)$$

where  $\Delta z/2 \approx 100$  m is the approximate level spacing of the simulations in the boundary layer. The regions where the criterion is satisfied are shown in yellow shadings in Figures 10(b),(c),(e),(f). The two simulations clearly show that at  $t = 90$  h, the CDI criterion is met at the precipitation base. Such a criterion has been applied with the total ice content, that is, with  $q_i$  being equal to the sum of cloud ice, snow and graupel mixing ratios. If the same computation is made by replacing  $q_i$  by the cloud ice mixing ratio only (not shown), the areas satisfying the CDI criterion entirely disappear. It confirms that the precipitating hydrometeors and their sublimation are the key for the destabilization of the air masses. In that sense, the CDI criterion in the present study cannot be thought as corresponding to the instability of the cloud base air masses only as it is closely related to the presence of precipitating hydrometeors.

Since variations of the Richardson number are dominated by fluctuations of the static stability in the region of interest, Figure 11 shows the static stability parameter. It is computed in two ways: one is  $N_v^2$  (Figures 11(a),(c)) and the other  $N_{i_v}^2 = (g/\theta_{i_v})(\partial\theta_{i_v}/\partial z)$  (Figures 11(a),(c)). For S1land,  $N_v^2$  is positive above the precipitation base and negative from the precipitation base down to the surface. In contrast, for S1land\_nocl, it is positive in a layer of few hundred meters below the precipitation base. As already mentioned, it reveals the cooling effect of sublimating hydrometeors. The main difference between  $N_v^2$  and  $N_{i_v}^2$  occurs at the precipitation base where the latter is negative. This corresponds to the yellow areas of Figure 10 and highlight the potential instability the air masses have if some precipitation is mixed with the more subsaturated air and sublimate. In other words, the negative values of  $N_v^2$  below the precipitation base correspond to the cooling of precipitation that happened before  $t = 90$  h while the negative values of  $N_{i_v}^2$  at the precipitation base correspond to the potential cooling effect of precipitation that may occur after  $t = 90$  h. In S1land\_nocl, negative values of  $N_{i_v}^2$  also appear at the precipitation base and the CDI criterion is also satisfied in that region. However, since the sublimation cooling is suppressed in that simulation, the instability cannot be released.

At  $t = 93$  h, once the convective cells have fully developed, the CDI criterion is almost not satisfied in the downstream vicinity of the cells (see cross section in Figure 12(b) and compare to the one shown in Figure 10(b)) and the static stability is not homogeneously negative anymore. It suggests that the first round of convective rolls have consumed the instabilities. At the same time, the CDI criterion is met more upstream of the first round of cells near the new cross section ZZ' (Figures 12(a),(c)). As mentioned earlier and shown in Figures 5(g),(h),(i), after  $t = 93$  h, a second round of convective cells appear. Therefore, our analysis suggests that the CDI and the convective instability below help to destabilize the air below the leading edge of the SJ first but also farther upstream at later times. This could explain the occurrence of the two clusters of convective cells.

To conclude, the criteria for CDI at the precipitation base and convective instability below the precipitation base are satisfied before the occurrence of the convective cells and disappear once they are fully mature, suggesting that the instabilities are consumed. Both instabilities are set by the cooling effect of sublimation and melting of snow and graupel hydrometeors. These sublimation and melting processes more easily happen, and the instabilities are more easily satisfied, at the leading edge of the sting jet because it is the region marked by advection of cloudy air above subsaturated air. It is still not clear if sublimation and melting of precipitating hydrometeors is triggered by mixing as required in the CDI theory. In that case, the mixing could be initiated because of the weak positive values of the Richardson number at the precipitation base. Another possibility is that sublimation and melting naturally occur once the precipitation falls into the subsaturated air.

## 4 | CONCLUSION

The present study investigates processes leading to the formation of maximum surface wind gusts within an idealized sting-jet cyclone simulated with the mesoscale model Meso-NH. A focus is made on surface wind gusts appearing between the head of the bent-back warm front and the cold front in a region of weak thermal contrasts. Different numerical simulations performed at different horizontal grid spacings with different surface roughness values show that surface winds ahead of the bent-back warm front and below the leading edge of the sting jet increase by increasing both the horizontal resolution and the surface roughness. For a given surface roughness, the intensity of these surface winds increases with resolution while the sting-jet intensity above the boundary layer stays almost the same. Only the 1-km grid-spacing simulation with typical land surface roughness (S1land) exhibits stronger surface winds ahead of the bent-back warm front than near the cold-conveyor-belt jet. For coarser resolution and/or weaker roughness, the maximum surface wind gusts occur below the cold-conveyor-belt jet.

The downward transfer of momentum in the boundary layer of the S1land simulation is organized by along wind convective rolls where the maximum surface wind gusts are correlated with the descending branches of the convective rolls. The correlation varies between 0.6 and 0.8 depending on the regions. Also, at the top of the boundary layer peaks in precipitation correspond to minima of horizontal wind speed and are co-located with the upper part of the ascending branches of the rolls. The distance between two consecutive bands of maximum surface winds typically varies between 5 km and 10 km. The S1land simulation rather adequately reproduces the multiple bands of strong surface wind speed reported in the literature for sting-jet cyclones. For instance, it brings similarities with the "St-Jude" or "Christian" storm studied by Browning et al. (2015) even though the spacing between the individual bands of maximum wind speed was found to be smaller for the real storm (between 500 m and 3 km).

Passive tracers initiated in the SJ region were computed to better understand how the momentum is transferred to the surface. The tracer can stay for few hours in the vicinity of the SJ near the top of the boundary layer without being transferred further downward. But once the descending branch of a convective roll approaches the region of high passive tracer content, a rapid downward transfer happens and in almost half an hour some passive tracer content is transported from the top of the boundary layer to the surface. Therefore, these are the resolved convective rolls that initiate and transport the tracer until reaching a few hundred meters above the surface. Then, the turbulent fluxes take over the downward transport of tracer and momentum in the last hundred meters of the atmosphere. More upstream, closer to the bent-back warm front, such convective activity is almost absent and the downward transfer of momentum much less efficient and less localized.

Then, the paper addressed the question of why such downward transfer of momentum by convective rolls happen below the leading edge of the sting jet in the vicinity of the head of the boundary-layer clouds. Before the formation of the convective rolls in S1land, we show this region is marked by low values of the Bulk Richardson number computed between the top of the boundary layer and the surface. These low values are not related to greater values of the wind shear but rather to lower values of the static stability. The static stability presents negative minima just below the precipitation base and stays negative down to the surface. Such a feature is identified as being due to the cooling due to sublimation and melting of snow and graupel near and below the cloud base. This is confirmed by turning off the cooling associated to these processes in a sensitivity experiment. In that simulation, the convective rolls completely disappear and the static stability is slightly positive in the few hundred meters below the precipitation base. It confirms that evaporating precipitation, mostly sublimation in the present case, is a key process for the downward transfer of momentum inside the boundary layer as suggested by Browning et al. (2015). It is also in good agreement with the role of evaporation in facilitating convection in the boundary layer as described in Browning and Smart (2018) in a different context. An analysis of the cloud-base detrainment instability (CDI) has been also performed showing that

479 the CDI criterion is satisfied before the occurrence of the convective cells and largely disappear once the cells are  
480 well formed, suggesting that the instability is consumed after a while. However, the CDI criterion has been applied  
481 to the sum of all ice species and such an instability is not satisfied in the present case by considering cloud ice only.  
482 The instability comes from the potential sublimation of snow and graupel. In that sense, it cannot be strictly seen as a  
483 pure cloud-base destabilization as precipitation must be taken into account. In the simulation where the evaporative  
484 cooling of precipitating hydrometeors is turned off, the CDI criterion is still satisfied but the instability cannot be  
485 released because it precisely requires sublimation and melting of ice. Our conclusion is that before the occurrence  
486 of the convective rolls, both criteria for CDI at the precipitation base and convective instability in the subsaturated  
487 air below are satisfied. Conditions for convective instability below the precipitation base are met because there was  
488 a cooling due to sublimation and melting of solid precipitation that led to that condition. Conditions for CDI at the  
489 precipitation base are met because there is the potential for subsequent cooling as soon as precipitation will be mixed  
490 with the subsaturated air below. Hence, our interpretation is that the convective rolls are formed by destabilization of  
491 the air masses at the precipitation base via CDI and the associated air masses continue their descent because they met  
492 favorable conditions for convective instability further below the precipitation base.

493 The present study provides new insights on the boundary-layer processes responsible for the downward transfer  
494 of momentum from the sting jet to the surface. One nice result is that it provides guidance of how to form multiple  
495 bands of strong surface winds below the leading edge of the sting jet in an idealized numerical set up. The two key  
496 identified parameters are horizontal resolution and surface roughness. We also show that, with a very simple setup  
497 of the boundary layer, it is possible to trigger mixing and downward transport of momentum just by destabilization of  
498 air masses from the top of the boundary layer. This strong vertical mixing by convective rolls was found in different  
499 observational studies (e.g., Parton et al., 2009; Browning et al., 2015) but not well represented or absent in simulations of  
500 real cases (Parton et al., 2009) or in simulations of idealized cases (Baker et al., 2014; Coronel et al., 2016). In the present  
501 study, we were able to represent this strong vertical mixing by convective plumes in our model and to identify the  
502 dominant processes that help to form such intense convective plumes. These are mainly the sublimation and melting of  
503 precipitating ice hydrometeors. We also show that, even though a 10–15 km horizontal grid spacing with a 200–300 m  
504 level spacing is enough to represent sting jets themselves (Clark and Gray, 2018), much higher resolution is required to  
505 accurately represent the downward transfer of momentum inside the boundary layer. The next step will be to consider  
506 a more realistic boundary layer that will include surface fluxes of heat and moisture by imposing a forcing by sea surface  
507 temperature. This will destabilize the boundary layer from below and this will also facilitate the downward transfer of  
508 momentum as shown in the real case study of Slater et al. (2017).

## 509 ACKNOWLEDGEMENTS

510 This work has been supported by the French national programme LEFE/INSU. The authors would like to acknowledge  
511 Suzanne Gray for fruitful discussions on various occasions over the course of this study and in particular for her  
512 suggestion of using passive tracers. We thank the two reviewers, David Schultz and an anonymous one, for their helpful  
513 comments that allowed us to significantly improve the paper.

## 514 REFERENCES

- 515 Baker, L., Gray, S. L. and Clark, P. A. (2014) Idealised simulations of sting-jet cyclones. *Quart. J. Roy. Meteor. Soc.*, **140**, 96–110.
- 516 Baker, L., Martinez-Alvarado, O., Methven, J. and Knippertz, P. (2013) Flying through extratropical cyclone friedhelm. *Weather*,  
517 **68**, 9–13.



- 518 Bechtold, P., Bazile, E., Guichard, F., Mascart, P. and Richard, E. (2001) A mass flux convection scheme for regional and global  
519 models. *Quart. J. Roy. Meteor. Soc.*, **127**, 869–886.
- 520 Bennetts, D. and Hoskins, B. J. (1979) Conditional symmetric instability - a possible explanation for frontal rainbands. *Quart. J.*  
521 *Roy. Meteor. Soc.*, **105**, 945–962.
- 522 Bougeault, P. and Lacarrère, P. (1989) Parameterization of orography-induced turbulence in a mesobeta-scale model. *Mon.*  
523 *Wea. Rev.*, **117**, 1872–1890.
- 524 Brâncus, M., Schultz, D. M., Antonescu, B., Dearden, C. and Stefan, S. (2019) Origin of strong winds in an explosive mediter-  
525 ranean extratropical cyclone. *Mon. Wea. Rev.*, **147**, 3649–3671.
- 526 Browning, K. A. (1990) *Organization of clouds and precipitation in extratropical cyclones*, vol. : extratropical cyclones, Erik Palmén  
527 memorial volume, chap. 8, 129–153. American Meteorological Society.
- 528 – (2004) The sting at the end of the tail: Damaging winds associated with extratropical cyclones. *Quart. J. Roy. Meteor. Soc.*,  
529 **130**, 375–399.
- 530 Browning, K. A. and Field, M. (2004) Evidence from meteosat imagery of the interaction of sting jets with the boundary layer.  
531 *Meteor. Appl.*, **11**, 277–289.
- 532 Browning, K. A. and Pardoe, C. (1973) Structure of low-level jet streams ahead of mid-latitude cold fronts. *Quart. J. Roy. Meteor.*  
533 *Soc.*, **99**, 619–638.
- 534 Browning, K. A. and Smart, D. J. (2018) Invigoration of convection by an overrunning diabatically modified cloud-top layer.  
535 *Quart. J. Roy. Meteor. Soc.*, **144**, 142–155.
- 536 Browning, K. A., Smart, D. J., Clark, M. R. and Illingworth, A. J. (2015) The role of evaporating showers in the transfer of sting-jet  
537 momentum to the surface. *Quart. J. Roy. Meteor. Soc.*, **141**, 2956–2971.
- 538 Carlson, T. (1980) Airflow through midlatitude cyclones and the comma cloud pattern. *Mon. Wea. Rev.*, 1498–1509.
- 539 Clark, P. A., Browning, K. and Wang, C. (2005) The sting at the end of the tail: Model diagnostics of fine-scale three-dimensional  
540 structure of the cloud head. *Quart. J. Roy. Meteor. Soc.*, **131**, 2263–2292.
- 541 Clark, P. A. and Gray, S. L. (2018) Sting jets in extratropical cyclones: a review. *Quart. J. Roy. Meteor. Soc.*, **144**, 943–969.
- 542 Coronel, B., Ricard, D., Rivière, G. and Arbogast, P. (2016) Cold-conveyor-belt jet, sting jet and slantwise circulations in ideal-  
543 ized simulations of extratropical cyclones. *Quart. J. Roy. Meteor. Soc.*, **182**, 1781–1796.
- 544 Cuxart, J., Bougeault, P. and Redelsperger, J. L. (2000) A turbulence scheme allowing for mesoscale and large-eddy simulations.  
545 *Quart. J. Roy. Meteor. Soc.*, **126**, 1–30.
- 546 Emanuel, K. A. (1981) A similarity theory for unsaturated downdrafts within clouds. *J. Atmos. Soc.*, **38**, 1541–1557.
- 547 – (1994) *Atmospheric convection*. Oxford University Press. 580 pp.
- 548 Gray, S. L., Martinez-Alvarado, O., Baker, L. H. and Clark, P. A. (2011) Conditional symmetric instability in sting-jet storms.  
549 *Quart. J. Roy. Meteor. Soc.*, **137**, 1482–1500.
- 550 Grønås, S. (1995) The seclusion intensification of the New Year's day storm 1992. *Tellus*, **47A**, 733–746.
- 551 Hart, N., Gray, S. and Clark, P. (2017) Sting-jet windstorms over the North Atlantic: climatology and contribution to extreme  
552 wind risk. *J. Climate*, **30**, 5455–5471.
- 553 Hewson, T. and Neu, U. (2015) Cyclones, windstorms and the imilast project. *Tellus A*, **67**, 27128.

- 554 Kanak, K. M., Straka, J. M. and Schultz, D. M. (2008) Numerical simulation of mammatus. *J. Atmos. Sci.*, **65**, 1606–1621.
- 555 Kelley, J. D., Schultz, D. M., Schumacher, R. and Durran, D. R. (2019) Can mountain waves contribute to damaging winds far  
556 away from the lee slope? *Wea. Forecasting*.
- 557 Lac, C., Chaboureau, P., Masson, V., Pinty, P., Tulet, P., Escobar, J., Leriche, M., Barthe, C., Aouizerats, B., Augros, C., Au-  
558 mond, P., Auguste, F., Bechtold, P., Berthet, S., Bieilli, S., Bosseur, F., Caumont, O., Cohard, J.-M., Colin, J. M., Couvreux,  
559 F., Cuxart, J., Delautier, G., Dauhut, T., Ducrocq, V., Filippi, J.-B., Gazen, D., Geoffroy, O., GHEUSI, F., Honnert, R., Lafore, P.,  
560 Lebeaupin Brossier, C., Libois, Q., Lunet, T., Mari, C., Maric, T., Mascart, P., Mogé, M., Molinié, G., Nuissier, O., Pantillon, F.,  
561 Peyrillé, P., Pergaud, J., Perraud, E., Pianezze, J., Redelsperger, J.-L., Ricard, D., Richard, E., Riette, S., Rodier, Q., Schoetter, R.,  
562 Seyfried, L., Stein, J., Suhre, K., Taufour, M., Thouron, O., Turner, S., Verrelle, A., Vié, B., Visentin, F., Vionnet, V. and Wautelet,  
563 P. (2018) Overview of the Meso-NH model version 5.4 and its applications. *Geoscientific Model Development Discussions*,  
564 1929–1969.
- 565 Lackmann, G. (2002) Cold-frontal potential vorticity maxima, the low-level jet, and moisture transport in extratropical cyc-  
566 clones. *Mon. Wea. Rev.*, 59–74.
- 567 Lafore, J.-P., Stein, J., Asencio, N., Bougeault, P., Ducrocq, V., Duron, J., Fischer, C., Hérelil, P., Mascart, P., Masson, V., Pinty, J.-P.,  
568 Redelsperger, J. L., Richard, E. and de Arellano, J. V.-G. (1998) The meso-nh atmospheric simulation system. part i: adiabatic  
569 formulation and control simulations. *Ann. Geophysicae*, **16**, 90–109.
- 570 Lean, H. W. and Clark, P. A. (2003) The effects of changing resolution on mesoscale modelling of line convection and slantwise  
571 circulations in fastex iop16. *Quart. J. Roy. Meteor. Soc.*, **129**, 2255–2278.
- 572 Martinez-Alvarado, O., Baker, L. H., Gray, S. L., Methven, J. and Plant, R. S. (2014a) Distinguishing the cold conveyor belt and  
573 sting jet airstreams in an intense extratropical cyclone. *Mon. Wea. Rev.*, **142**, 2571–2595.
- 574 Martinez-Alvarado, O., Gray, S., Hart, N., P.A. Clark, K. H. and Roberts, M. (2018) Increased wind risk from sting-jet windstorms  
575 with climate change. *Environ. Res. Lett.*, **13**, 044002.
- 576 Martinez-Alvarado, O., Gray, S. L., Catto, J. L. and Clark, P. A. (2012) Sting jets in intense winter north-atlantic windstorms.  
577 *Environ. Res. Lett.*, **7**, 024014, doi: 10.1088/1748-9326/7/2/024014.
- 578 – (2014b) Corrigendum: Sting jets in intense winter north-atlantic windstorms (2012 environmental research letters 7,  
579 024014). *Environ. Res. Lett.*, **9**, 039501, doi: 10.1088/1748-9326/9/3/039501.
- 580 Martinez-Alvarado, O., Weidle, F. and Gray, S. L. (2010) Sting jets in simulations of a real cyclone by two mesoscale models.  
581 *Mon. Wea. Rev.*, **138**, 4054–4075.
- 582 Parton, G., Vaughan, G., Norton, E. G., Browning, K. A. and Clark, P. A. (2009) Wind profiler observations of a sting jet. *Quart. J.*  
583 *Roy. Meteor. Soc.*, **135**, 663–680.
- 584 Persson, P. O. G. and Warner, T. T. (1993) Nonlinear hydrostatic conditional symmetric instability: Implications for numerical  
585 weather prediction. *Quart. J. Roy. Meteor. Soc.*, **121**, 1821–1833.
- 586 Pinty, J.-P. and Jabouille, P. (1998) A mixed-phase cloud parameterization for use in a mesoscale non-hydrostatic model: Sim-  
587 ulations of a squall line and of orographic precipitations, in paper presented at conference on cloud physics, *Am. Meteorol.*  
588 *Soc.*, Everett, WA. 217–220.
- 589 Rivière, G., Arbogast, P. and Joly, A. (2015a) Eddy kinetic energy redistribution within idealized extratropical cyclones using a  
590 two-layer quasi-geostrophic model. *Quart. J. Roy. Meteor. Soc.*, **141**, 207–223.
- 591 – (2015b) Eddy kinetic energy redistribution within windstorms *Klaus* and *Friedhelm*. *Quart. J. Roy. Meteor. Soc.*, **141**, 925–938.
- 592 Schultz, D. (2001) Reexamining the cold conveyor belt. *Mon. Wea. Rev.*, 2205–2225.
- 593 Schultz, D. and Browning, K. A. (2017) What is a sting jet? *Weather*, **72**, 63–66, doi: 10.1002/wea.2795.

- 594 Schultz, D. and Sienkiewicz, J. (2013) Using frontogenesis to identify sting jets in extratropical cyclones. *Wea. Forecasting*, **28**,  
595 603–613.
- 596 Schultz, D. M. and Schumacher, P. N. (1999) The use and misuse of conditional symmetric instability. *Mon. Wea. Rev.*, **127**,  
597 2709–2732, Corrigendum 128: 1573.
- 598 Shapiro, M. and Keyser, D. (1990) *Fronts, jet streams and the tropopause*, vol. Extratropical cyclones, Newton and Holopainen  
599 eds, chap. 10, 167–191. American Meteorological Society.
- 600 Slater, T., Schultz, D. and Vaughan, G. (2015) Acceleration of near-surface strong winds in a dry, idealized extratropical cyclone.  
601 *Quart. J. Roy. Meteor. Soc.*, **141**, 1004–1016.
- 602 – (2017) Near-surface strong winds in a marine extratropical cyclone: acceleration of the winds and the importance of surface  
603 fluxes. *Quart. J. Roy. Meteor. Soc.*, **143**, 321–332.
- 604 Smart, D. and Browning, K. (2014) Attribution of strong winds to a cold conveyor belt and sting jet. *Quart. J. Roy. Meteor. Soc.*,  
605 **140**, 595–610.
- 606 Vaughan, G., Methven, J. and co authors (2015) Cloud banding and winds in intense European cyclones: Results from the  
607 DIAMET project. *Bull. Amer. Meteor. Soc.*, **96**, 249–265.
- 608 Volonté, A., Clark, P. A. and Gray, S. L. (2018) The role of mesoscale instabilities in the sting-jet dynamics of windstorm *tini*.  
609 *Quart. J. Roy. Meteor. Soc.*, **144**, 877–899.

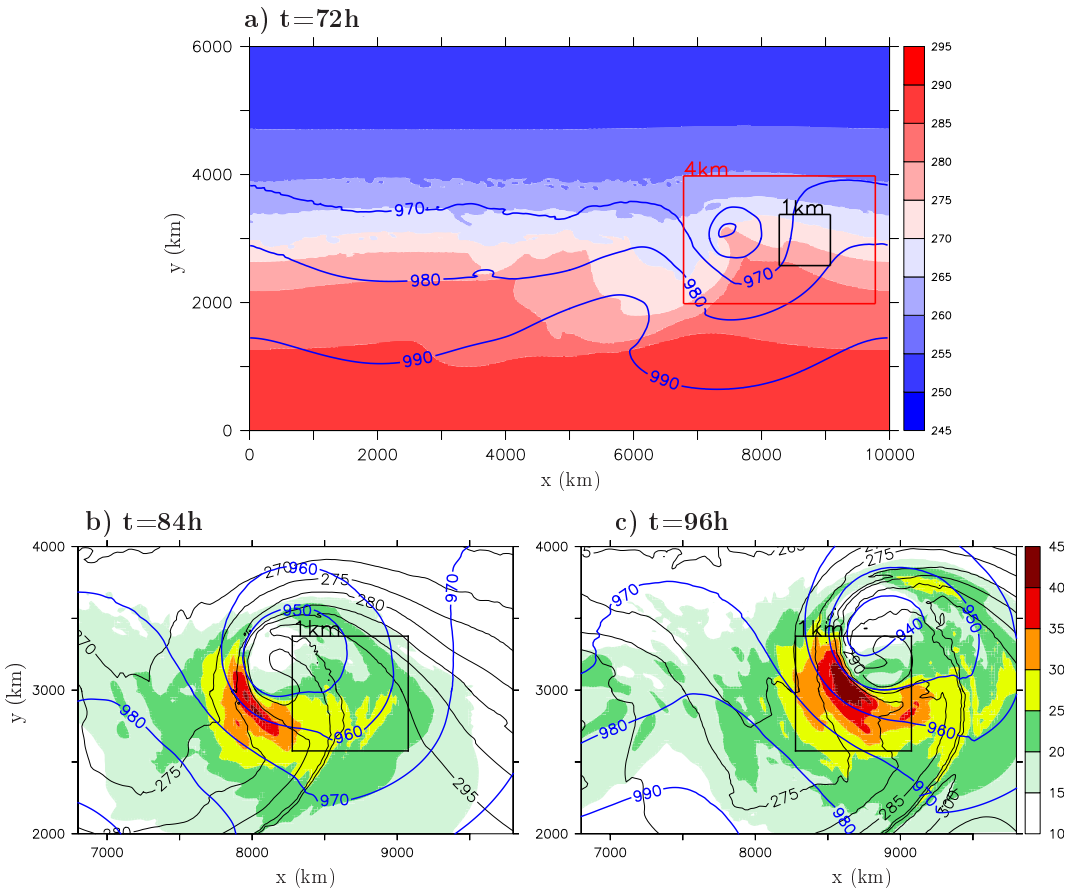


**FIGURE 1** (a) Initial state of S20land, S20sea, S4land, S4sea experiments: the temperature field at  $z = 25\text{ m}$  is represented in shadings (units: K), the pressure at  $z = 25\text{ m}$  in blue contours (interval: 10 hPa). (b),(c) Horizontal wind speed at  $z = 1.6\text{ km}$  (shadings; units:  $\text{m s}^{-1}$ ), sea level pressure (blue contours; interval: 10 hPa), and equivalent potential temperature at  $z = 1.6\text{ km}$  (black contours; interval: 5 K) for the simulation S20land for (a)  $t = 84\text{ h}$  and (b)  $t = 96\text{ h}$ . The black square corresponds to the domain of the 1-km grid spacing simulations.

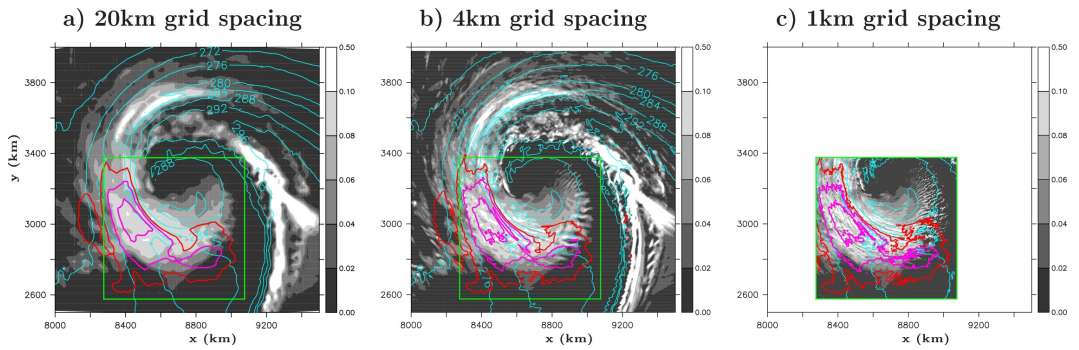


**FIGURE 2** Maximum of the sum of cloud liquid and ice water contents between  $z = 0.5 \text{ km}$  and  $z = 2.0 \text{ km}$  (grey shadings; units:  $\text{g kg}^{-1}$ ), horizontal wind speed at  $z = 1.6 \text{ km}$  ( $30 \text{ m s}^{-1}$  in red and 35 and  $40 \text{ m s}^{-1}$  in magenta), and equivalent potential temperature at  $z = 1.6 \text{ km}$  (light blue contours; interval: 4 K) at  $t = 93 \text{ h}$  for different simulations: (a) S20land, (b) S4land and (c) S1land.

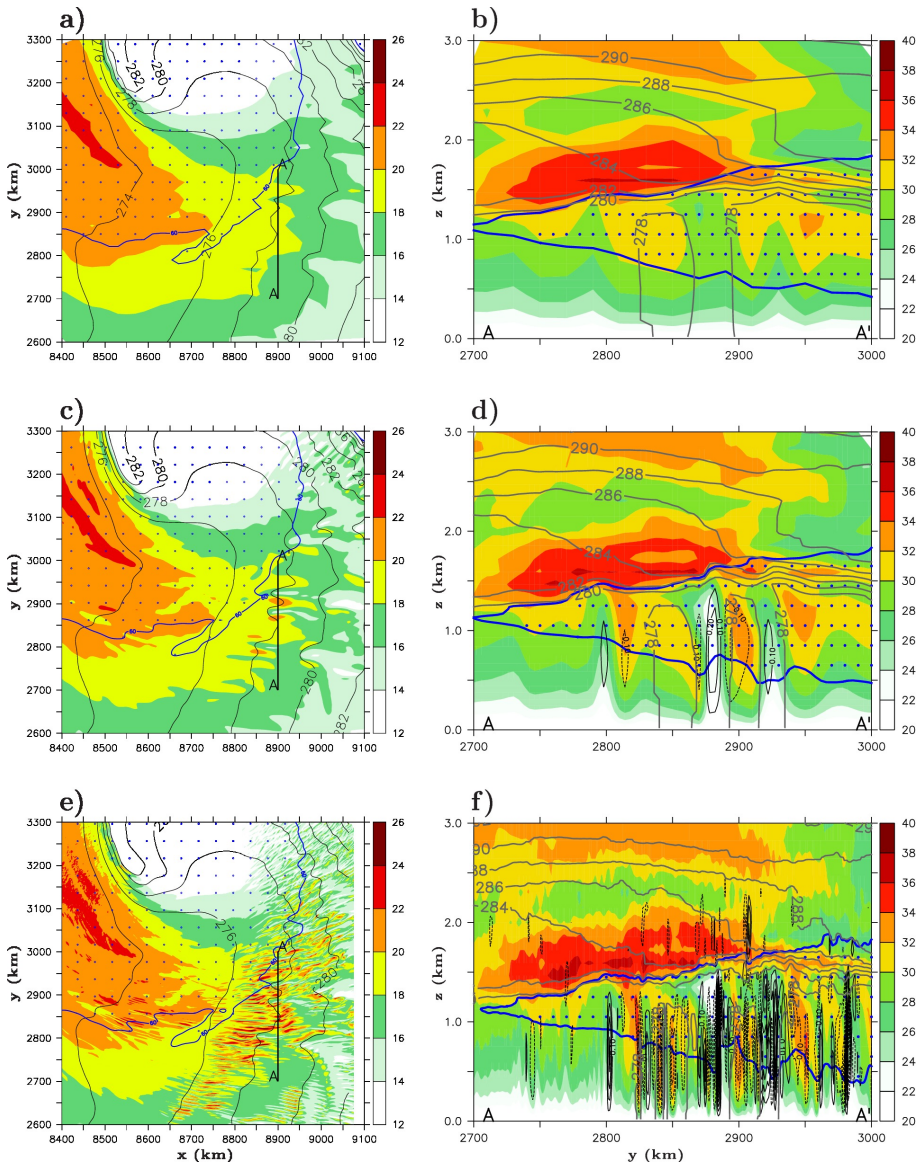


**FIGURE 3** (Left column) Horizontal wind speed (shadings; units:  $\text{m s}^{-1}$ ), relative humidity greater than 60% (blue contour and stippled areas), and equivalent potential temperature at  $z = 25$  m (black contour; interval: 2 K) at  $t = 93$  h. The latter two fields are smoothed for the 4-km and 1-km grid-spacing simulations but not the wind speed. (Right column) Vertical cross section of the horizontal wind speed (shadings; units:  $\text{m s}^{-1}$ ), 80% relative humidity (blue contour), equivalent potential temperature (magenta contour; interval: 2 K) and vertical velocity (black dashed and solid contours for negative and positive values respectively; interval:  $0.1 \text{ m s}^{-1}$ ). Simulations with land roughness: (upper panels) S20land, (middle panels) S4land and (lower panels) S1land.

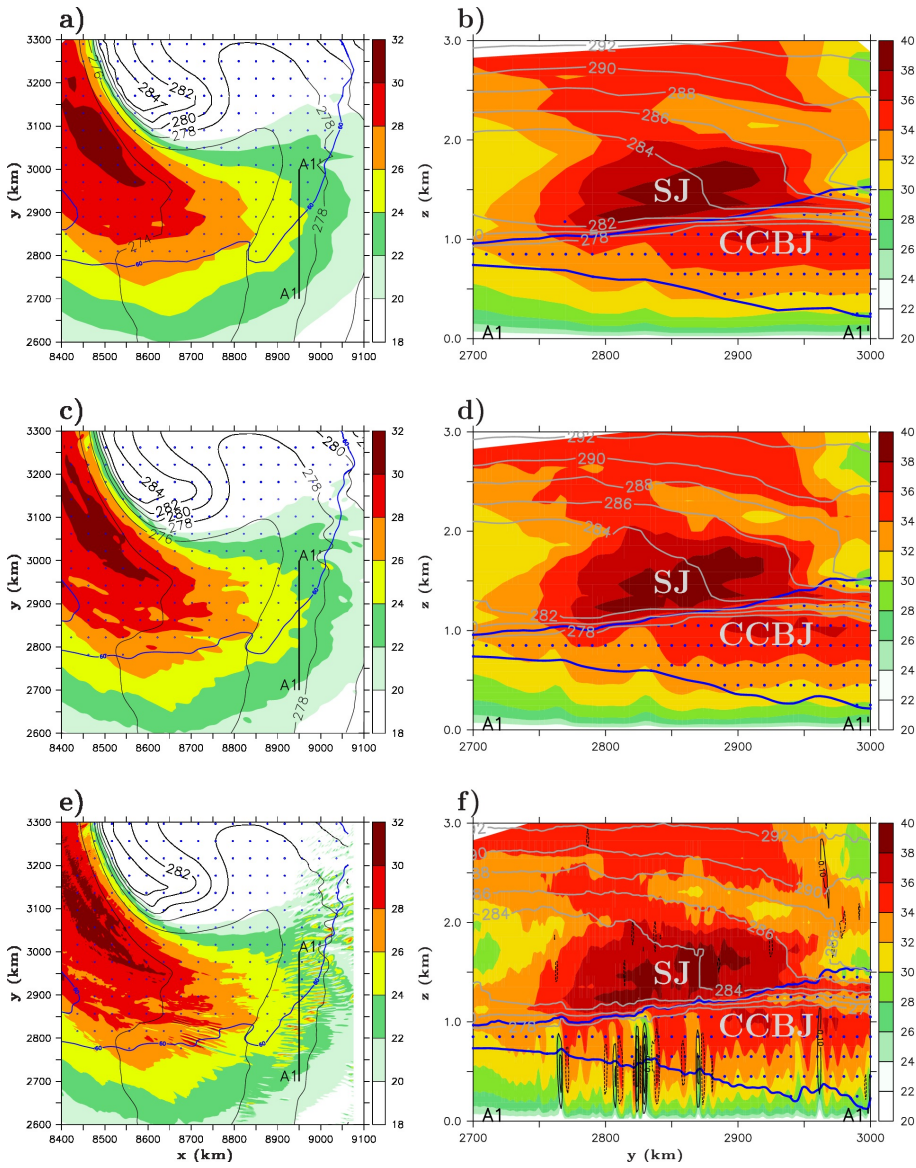


**FIGURE 4** Same as Figure 3 but for simulations with sea surface roughness: (upper panels) S20sea, (middle panels) S4sea and (lower panels) S1sea. Note that the vertical cross sections A1A1' are 50 km ahead of the vertical cross sections AA' shown in Figure 3 to select the small-scale bands of near-surface wind speed maxima. SJ and CCBJ correspond to the sting jet and cold-conveyor-belt jet locations, respectively.

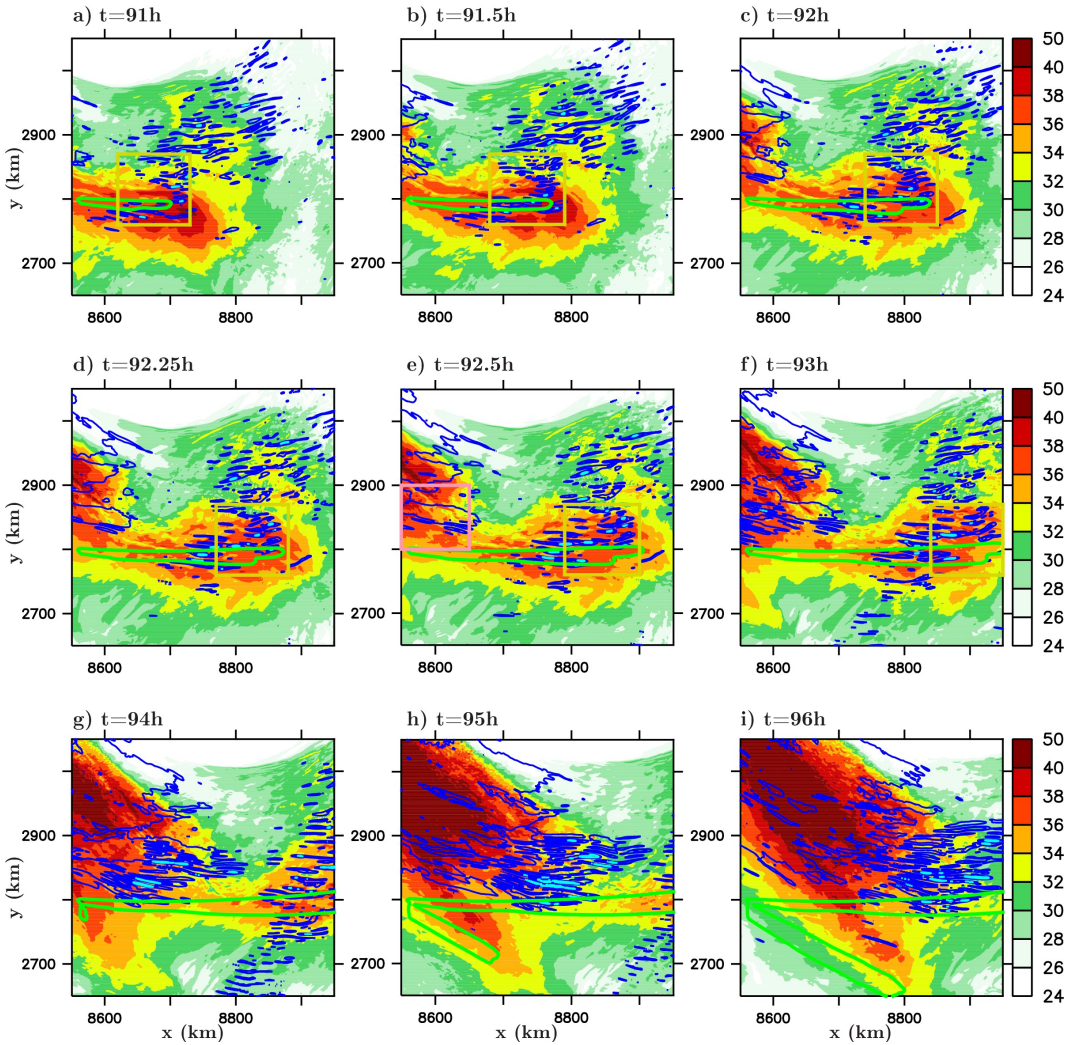


**FIGURE 5** Horizontal wind speed at  $z = 1.6$  km (shadings; units:  $\text{m s}^{-1}$ ) and  $z = 200$  m ( $28$  and  $30$   $\text{m s}^{-1}$  in blue contours and  $32$   $\text{m s}^{-1}$  in light blue contours) at (a)  $t = 91$  h, (b)  $t = 91.5$  h, (c)  $t = 92$  h, (d)  $t = 92.25$  h, (e)  $t = 92.5$  h, (f)  $t = 93$  h, (g)  $t = 94$  h, (h)  $t = 95$  h, and (i)  $t = 96$  h for S1land. The thick green contour corresponds to a given value of the passive tracer injected around  $x = 8550$  km and  $y = 2800$  km. The yellow squares are zoomed areas shown in Figure 6.



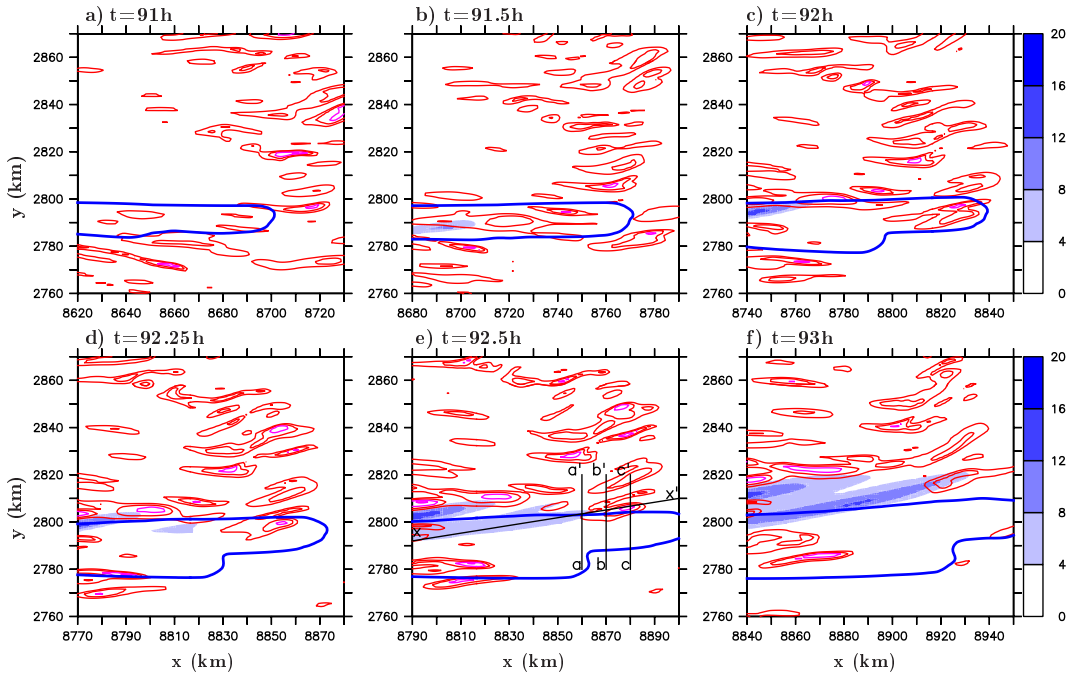


**FIGURE 6** Passive tracer at  $z = 500$  m (shadings) and  $z = 1.6$  km (blue contour; value equals to 50), horizontal wind speed at  $z = 200$  m ( $28$  and  $30 \text{ m s}^{-1}$  in red contours and  $32 \text{ m s}^{-1}$  in magenta contours) at (a)  $t = 91$  h, (b)  $t = 91.5$  h, (c)  $t = 92$  h, (d)  $t = 92.25$  h, (e)  $t = 92.5$  h and (f)  $t = 93$  h for the zoomed areas shown in Figures 5(a)-(f).

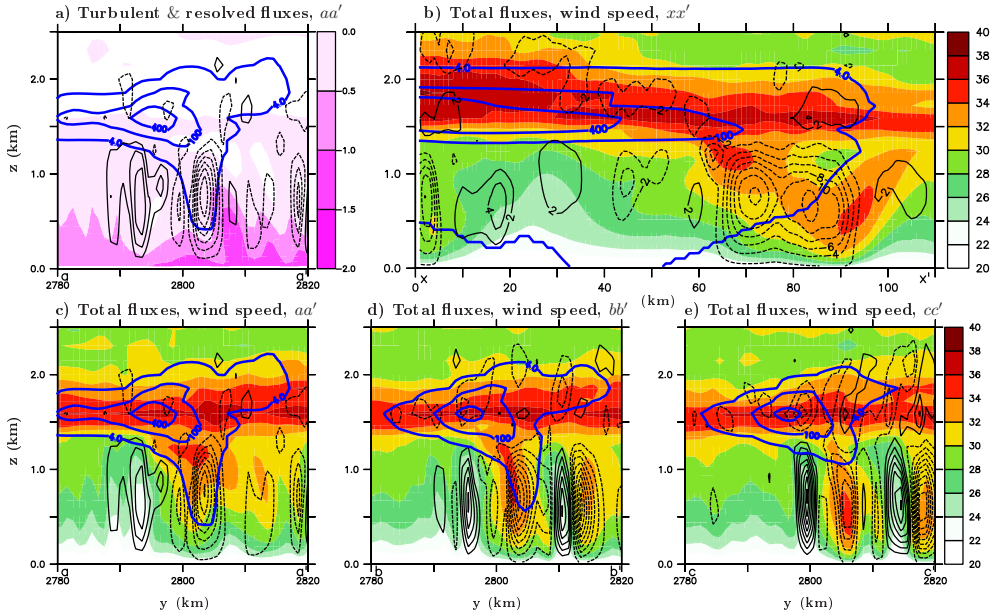


**FIGURE 7** Vertical cross sections at  $t = 92.5$  h shown in Figure 6(e). (a) cross section aa' of the vertical turbulent fluxes of zonal momentum (shadings; units:  $\text{m}^2\text{s}^{-2}$ ), resolved vertical fluxes of zonal momentum (black dashed and solid contours for negative and positive values; interval:  $2 \text{ m}^2\text{s}^{-2}$ ) and passive tracer (blue contour for a given value of 4). (b) cross section xx' of horizontal wind speed (shadings; units:  $\text{m s}^{-1}$ ), total vertical fluxes of zonal momentum (black dashed and solid contours for negative and positive values; interval:  $2 \text{ m}^2\text{s}^{-2}$ ) and passive tracer (blue contours for 4, 100 and 400 values). (c), (d) and (e) same as in (b) but for the cross sections aa', bb' and cc' respectively.

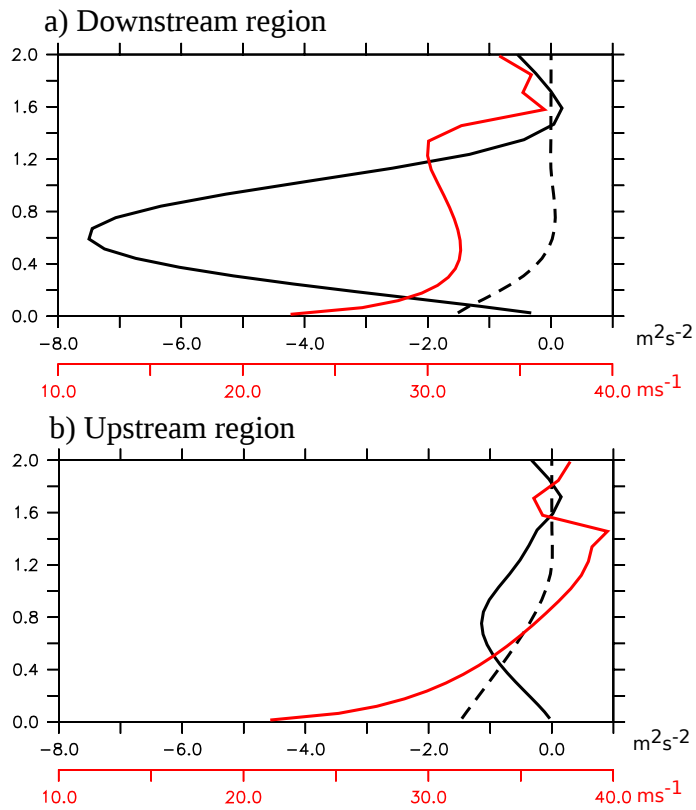


**FIGURE 8** Vertical profiles of horizontal wind speed (red) and resolved (solid black) and turbulent (dash black) vertical fluxes of zonal momentum at  $t = 92.5$  h in (a) downstream and (b) upstream regions shown respectively by the yellow and pink squares in Figure 5(e) where horizontal wind speed at  $z = 200$  m exceeds  $28 \text{ m s}^{-1}$ .

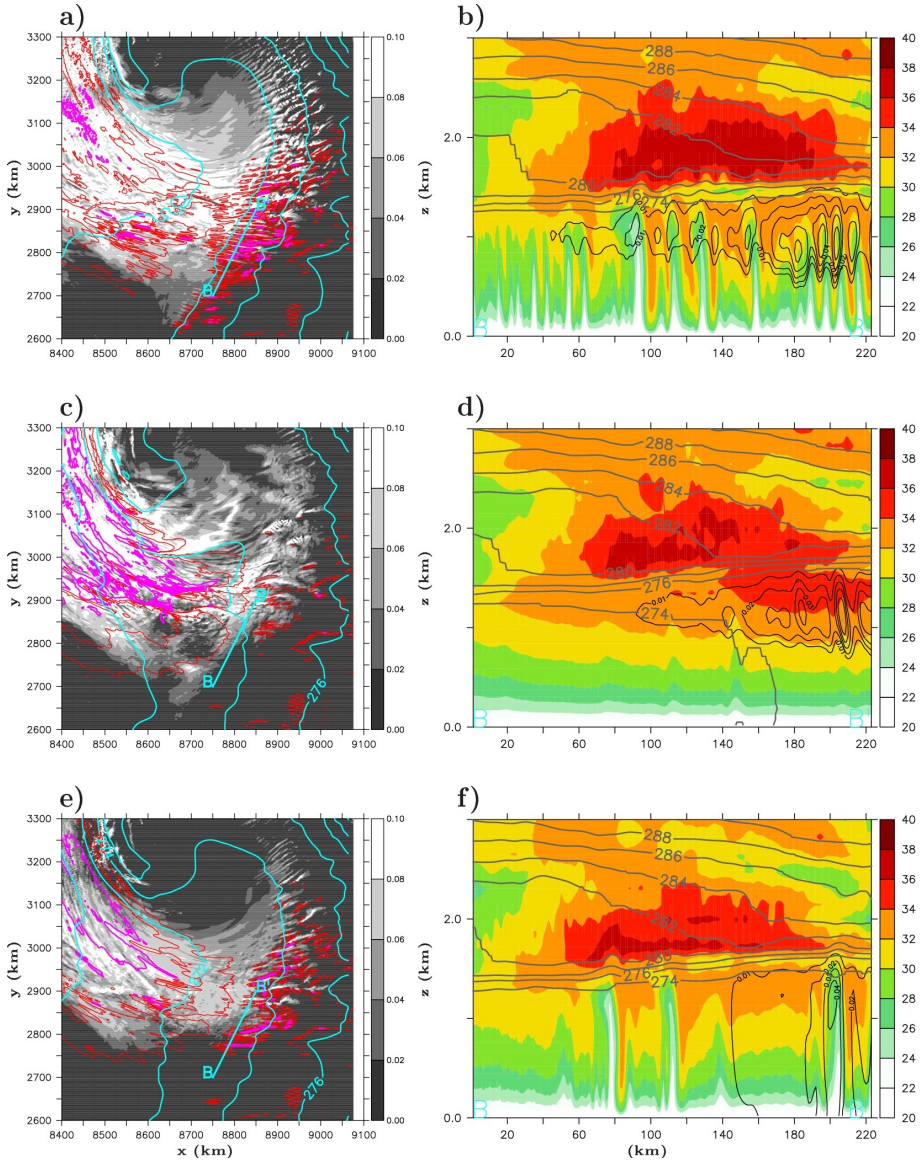


**FIGURE 9** (Left column) Maximum of the sum of cloud liquid and ice water contents between  $z = 0.0$  km and  $z = 2.0$  km (grey shadings; units:  $\text{g kg}^{-1}$ ), surface wind gusts ( $28$  and  $30 \text{ m s}^{-1}$  in red contours and  $32$  and  $34 \text{ m s}^{-1}$  in magenta contours), and potential temperature at  $z = 25$  m (light blue contours; interval:  $2 \text{ K}$ ) at  $t = 93$  h. The surface wind gusts is a linear function of the  $10\text{-m}$  wind speed and the square root of the  $10\text{-m}$  turbulent kinetic energy. The temperature field is spatially smoothed for clarity purposes. (Right column) Vertical cross sections BB' of the total precipitation (sum of snow, graupel and rain mixing ratios in black contours; int:  $0.01 \text{ g kg}^{-1}$ ), horizontal wind speed (shadings; units:  $\text{m s}^{-1}$ ), and potential temperature (grey contours: interval:  $2 \text{ K}$ ). (Upper panels) S1land, (middle panels) S1land\_nocl, (lower panels) S1land\_nocl\_noevap.

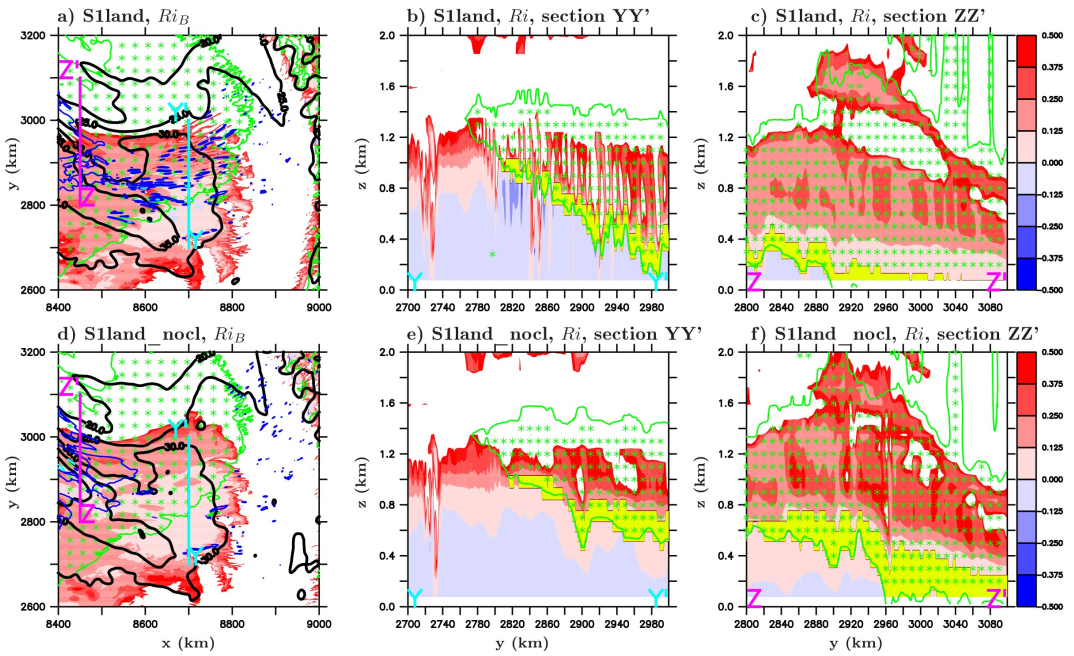


**FIGURE 10** (a), (d) Bulk Richardson number computed between  $z = 0.1$  km and  $z = 1.2$  km (shadings), horizontal wind speed at  $z = 1.6$  km (black contours; int:  $5 \text{ m s}^{-1}$  and a spatial smoothing is applied for clarity purposes) and  $z = 200$  m ( $28$  and  $30 \text{ m s}^{-1}$  in blue contours and  $32 \text{ m s}^{-1}$  in light blue contours), and ice water content (sum of cloud ice, snow and graupel) greater than  $5 \cdot 10^{-3} \text{ g kg}^{-1}$  (green contours with asterisks). (b), (e) Vertical cross sections YY' of the Richardson number (shadings), ice water content (sum of cloud ice, snow and graupel) greater than  $5 \cdot 10^{-3} \text{ g kg}^{-1}$  (green contours with asterisks). The yellow areas correspond to areas where CDI is satisfied. (c), (f) same as (b), (e) but for the cross section ZZ'. (Upper panels) S1land, (lower panels) S1land\_nocl. All panels are computed at  $t = 90$  h. Note that regions where the Richardson number exceeds 0.5 are in white.

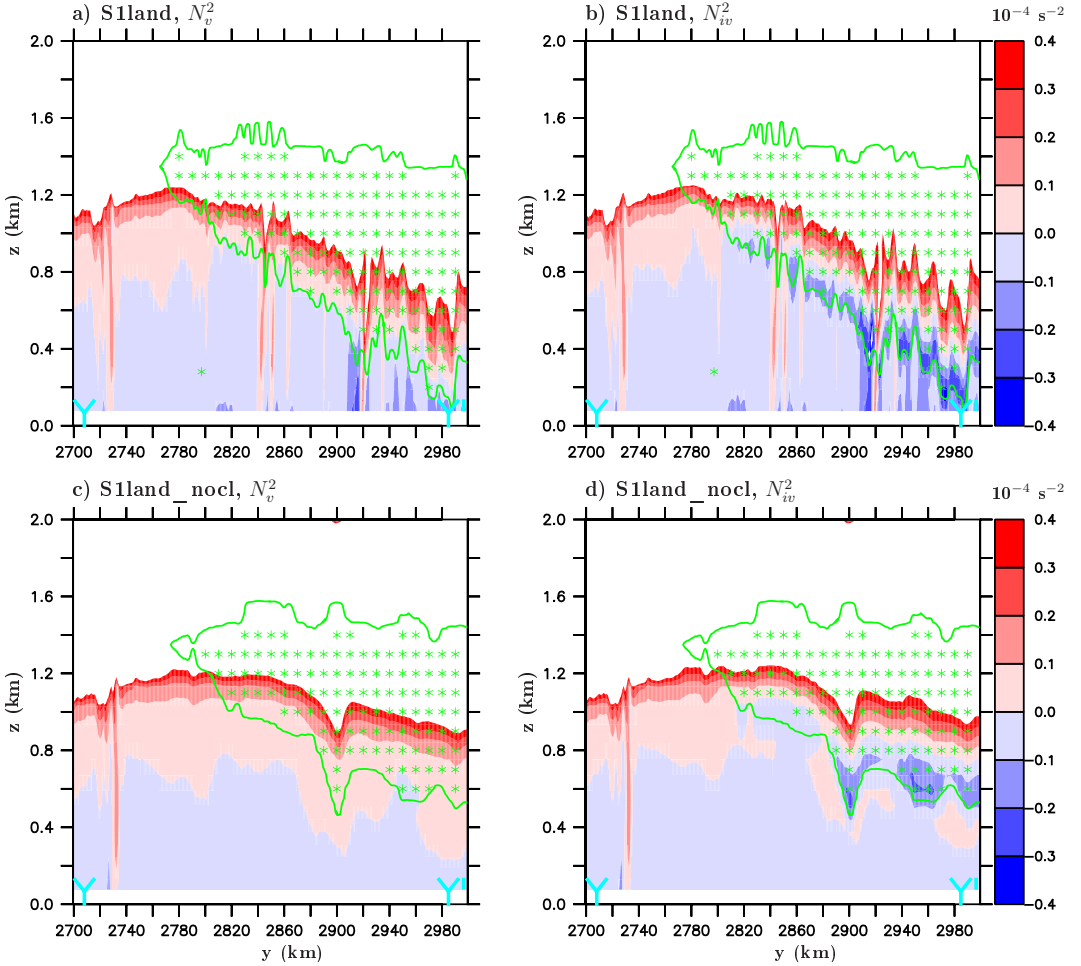


**FIGURE 11** Vertical cross sections  $YY'$  of the square of the static stability (shadings; units:  $\text{s}^{-2}$ ) for (a),(b) S1land and (c),(d) S1land\_nocl at  $t = 90$  h computed in two ways: (a), (c)  $N_v^2 = (g/\theta_v)(\partial\theta_v/\partial z)$  and (b), (d)  $N_{iv}^2 = (g/\theta_{iv})(\partial\theta_{iv}/\partial z)$ . The ice water content (sum of cloud ice, snow and graupel) greater than  $5 \times 10^{-3} \text{ g kg}^{-1}$  is represented in green contours with asterisks.

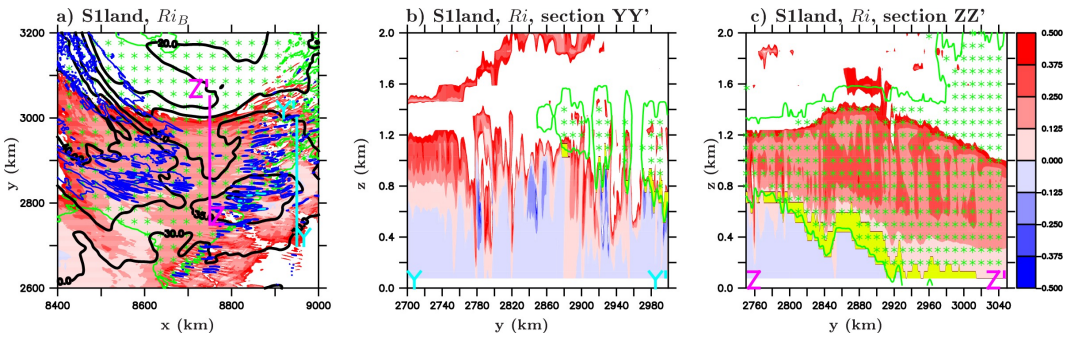


**FIGURE 12** Same as Figures 10(a)-(c) but at  $t = 93$  h.